HAL open science

Evaluating Marine Stratocumulus Clouds in the CNRM-CM6-1 Model Using Short-Term Hindcasts

Florent Brient, Romain Roehrig, Aurore Voldoire

▶ To cite this version:

Florent Brient, Romain Roehrig, Aurore Voldoire. Evaluating Marine Stratocumulus Clouds in the CNRM-CM6-1 Model Using Short-Term Hindcasts. Journal of Advances in Modeling Earth Systems, 2019, 11 (1), pp.127-148. 10.1029/2018MS001461 . hal-03416450

HAL Id: hal-03416450
https://hal.science/hal-03416450

Submitted on 10 Nov 2021

HAL is a multi-disciplinary open access archive for the deposit and dissemination of scientific research documents, whether they are published or not. The documents may come from teaching and research institutions in France or abroad, or from public or private research centers.

L'archive ouverte pluridisciplinaire **HAL**, est destinée au dépôt et à la diffusion de documents scientifiques de niveau recherche, publiés ou non, émanant des établissements d'enseignement et de recherche français ou étrangers, des laboratoires publics ou privés.

Distributed under a Creative Commons Attribution - NonCommercial - ShareAlike 4.0 International License

Check for updates

AGU100 ADVANCING EARTH AND SPACE SCIENCE

Journal of Advances in Modeling Earth Systems

RESEARCH ARTICLE

10.1029/2018MS001461

Evaluating Marine Stratocumulus Clouds in the CNRM-CM6-1 Model Using Short-Term Hindcasts

Florent Brient[1], **Romain Roehrig**[1], **and Aurore Voldoire**[1]

[1]CNRM, Université de Toulouse, Météo-France, CNRS, Toulouse, France

Key Points:

- Short-term hindcasts help to disentangle timescales of marine stratocumulus cloud bias growth in the CNRM-CM6-1 model
- Biases in low clouds are mostly related to errors in the subgrid distribution of temperature and humidity and the cloud-top entrainment
- Along with single-columns models, short-term hindcasts are a complementary testbed for cloud parameterization development

Correspondence to:
F. Brient,
florent.brient@gmail.com

Citation:
Brient F., Roehrig, R., & Voldoire, A. (2019). Evaluating marine stratocumulus clouds in the CNRM-CM6-1 model using short-term hindcasts. *Journal of Advances in Modeling Earth Systems*, *11*, 127–148. https://doi.org/10.1029/2018MS001461

Received 30 JUL 2018
Accepted 7 DEC 2018
Accepted article online 28 DEC 2018
Published online 17 JAN 2019

©2018. The Authors.
This is an open access article under the terms of the Creative Commons Attribution-NonCommercial-NoDerivs License, which permits use and distribution in any medium, provided the original work is properly cited, the use is non-commercial and no modifications or adaptations are made.

Abstract The representation of stratocumulus by the atmospheric component of the Centre National de Recherches Météorologiques model version 6 (CNRM-CM6-1) is assessed. An Atmospheric Model Intercomparison Project-type simulation is first used to document the main model errors, namely, a large lack of stratocumulus over the eastern part of tropical ocean basins. Short-term hindcasts, following the Transpose-Atmospheric Model Intercomparison Project framework, are then used to better assess the timescales associated with the cloud bias growth and to highlight the processes leading to them. These biases are shown to appear within only a few hours, independently of errors in the large-scale circulation that set up within a few days. Key processes underlying the low-cloud formation are thus mainly local and, to the first order, do not imply any feedback between the model physics and the large-scale dynamics. As a consequence, short-term hindcasts provide a relevant framework to investigate whether the low-cloud underestimate is related to errors in the large-scale state variables or to errors in the model parameterizations. Sensitivity tests highlight that the involved processes arise (1) mostly from misrepresentation of subgrid effects on cloud formation and (2) partly from biases in drying induced by cloud-top entrainment mixing. Improvements in the representation of stratocumulus in the CNRM-CM6-1 model might thus be expected by including a more realistic subgrid-scale temperature and moisture distribution, that would link convective and turbulence processes. Finally, this study confirms the potential of short-term hindcasts, which provide a trustworthy framework to evaluate and develop climate model parameterizations.

1. Introduction

Stratocumulus clouds prevail over the eastern parts of tropical ocean basins, where the large-scale subsiding atmosphere flow brings dry and warm air downward and ocean upwellings bring cold water upward. This generates stable atmospheric conditions associated with sharp inversions of humidity and temperature at the top of the boundary layer, which favor condensation and thus cloud formation within the first few kilometers (Klein & Hartmann, 1993; Lilly, 1968; Wood & Bretherton, 2006). These low clouds cover large oceanic areas and reflect large amounts of incoming solar radiation back to space. This makes them play a significant role on the global energy budget (Chen et al., 2000; Hartmann et al., 1992).

The formation of marine stratocumulus results from a subtle equilibrium between surface sensible and latent heat fluxes, boundary-layer mixing of humidity and temperature, microphysical processes, precipitation, cloud-top radiative cooling, and entrainment (Wood, 2012). The westward offshore increase in surface temperature and weakening of the large-scale subsidence amplify the vertical mixing and deepen the planetary boundary layer (PBL), which induce a transition from stratus and stratocumulus to trade-wind shallow cumulus cloud regimes (Bretherton & Wyant, 1997). The latter cloud regime is mainly driven by the surface buoyancy flux, while the first regime arises mostly from downward motions driven by cloud-top entrainment associated with radiative and evaporative cooling processes (Caldwell et al., 2005; Nicholls, 1984, 1989). The subtle boundary-layer interactions between the dynamics, the condensation, and the radiation need to be properly captured by climate models to accurately simulate marine low clouds.

The difficulty in representing subtropical stratocumulus in climate models has been pinpointed for a long time (Dal Gesso et al., 2015; Mechoso et al., 2014; Nam et al., 2012). Most climate models suffer from a lack of stratocumulus, which leads to overestimate the amount of solar radiation reaching the surface over the eastern part of tropical oceans (De Szoeke et al., 2012). This error has been highlighted as one of the causes of the systematic warm surface bias of climate models (De Szoeke et al., 2010; Hourdin et al., 2015;

Richter, 2015). Furthermore, errors in representing low clouds drive uncertainties in cloud feedbacks to global warming and thus in climate change projections (Brient et al., 2016; Bony & Dufresne, 2005; Tsushima et al., 2016). Any improvement in the representation of stratocumulus clouds would significantly improve the realism of ocean-atmosphere coupled climate simulations.

This difficulty in representing marine stratocumulus lies in the inability of climate models to accurately represent turbulent and cloud processes located within the few tens of meters below the top of the boundary layer and their interactions with the subcloud mixed layer. The coarse horizontal resolution of climate models calls for empirical formulations (parameterizations) to represent the effect of subgrid-scale cloud processes (turbulence, convection, microphysics) on the larger scales. These assumptions are often not appropriate to fully capture the balance of processes within stratocumulus-capped boundary layers (Moeng & Stevens, 2000; Siebesma et al., 2003), as well as their interaction with the model numerics (Bretherton et al., 2004). The vertical grid resolution of climate models is also often too coarse (50 – 100 m) to allow them to capture the strong inversion of the moisture and temperature profiles and the small-scale processes occurring there (Mellado, 2017). Numerical assumptions are sometimes used to reconstruct these inversions for use in parameterizations (e.g., Grenier & Bretherton, 2001).

Despite these difficulties, significant improvements have been made in the past two decades in the representation of stratocumulus processes in climate models. For instance, Lock et al. (2000) developed a boundary-layer scheme, which accounts for local and nonlocal turbulence productions (driven by both surface fluxes and cloud-top processes) in a set of cloud situations. Each of them are related to prescribed assumptions of turbulence exchange coefficients defined by the atmosphere stability and induce different subgrid turbulent fluxes. Additionally, a first-order turbulence closure involving parameterization of cloud-top entrainment is added (Lock, 1998). Implementing this boundary-layer scheme has led to significant improvements in the representation of clouds in the HadGEM model (Martin et al., 2006). More recently, Bretherton and Park (2009) proposed a boundary-layer scheme that also uses local and nonlocal turbulence assumptions for diffusivity profiles, but based on turbulent kinetic energy (TKE) equations. Particular care has been taken to accurately identify the height of the boundary layer. As in Lock et al. (2000), nonlocal cloud-top turbulence is also calculated by a parameterization of cloud-top entrainment (Bretherton et al., 2004; Grenier & Bretherton, 2001). These modifications also suggest better simulations of low-cloud transitions. Additionally, interactions between the subgrid turbulent processes and other parameterizations need to be addressed with care (e.g., Lock, 2001). In this regard, recent attempts have been undertaken to develop unified approaches for the representation of the boundary-layer mixing by both turbulent and convective processes and its coupling with cloud and condensation processes (Köhler et al., 2011; Siebesma et al., 2007; Sušelj et al., 2013; Tan et al., 2018).

To assess and improve parameterizations, single-column models (SCMs) are widely used (Betts & Miller, 1986; Lock et al., 2000; Randall et al., 1996). SCMs are usually run using idealized initial states and large-scale forcings (e.g., Duynkerke et al., 2004). While the SCM approach might be able to reproduce a diversity of cloud regimes, it does not allow to address the interactions between the model physics and the larger scales. This requires intermediate model configurations to fill the gap between the few available SCM configurations and the full 3-D model.

Here we propose to use short-term atmospheric hindcasts to address this gap. In the climate modeling community, this approach is often referred to as Transpose-Atmospheric Model Intercomparison Project (AMIP; Ma et al., 2014; Phillips et al., 2004; Williams et al., 2013). The hindcasts are initialized from realistic conditions, and their drift toward the model climatology can be analyzed to highlight mechanisms responsible for model errors (Toniazzo & Woolnough, 2014; Vannière et al., 2014; Voldoire et al., 2014; Wan et al., 2014) and identify physical processes that explain them (Ahlgrimm et al., 2018; Hannay et al., 2009; Morcrette et. al 2012; Zheng et al., 2016, 2017). The drift analysis also helps to disentangle the role of various processes and of their interaction with the large-scale dynamics, as they often have different time scales. Short-term hindcasts are an intermediate tool between SCM and long-term 3-D simulations: as in SCM, they allow us to focus on the local biases before the large-scale feedbacks start acting, while remaining cheaper than AMIP-type simulations. Additionally, this framework provides a wide set of atmospheric conditions to assess parameterizations, much larger than the few case studies available for SCMs. Despite these advantages, it seems that only a few studies have used the Transpose-AMIP framework to investigate in detail the physical processes leading to the stratocumulus biases. For instance, Hannay et al. (2009) and Medeiros et al. (2012) provide a process-oriented analysis of the diurnal cycle of marine stratocumulus. Using a cloud liquid water budget, the latter attributes the 5-day evolution of the CAM4 and CAM5 models stratocumulus bias to the boundary-layer parameterization (cloud-top radiative cooling, entrainment, and detrainment). They prove the usefulness of the Transpose-AMIP framework to disentangle structural and parametric uncertainties leading the stratocumulus biases (e.g., critical relative humidity threshold, entrainment efficiency).

In the present analysis, we aim to evaluate stratocumulus clouds simulated by the new version of the Centre National de Recherches Météorologiques (CNRM) model (CNRM-CM6-1) and further address the origin of their biases. The previous version of the climate model (CNRM-CM5) suffered from one of the largest underestimation in subtropical low clouds among climate models (Nam et al., 2012), which partly drives the strong warm surface biases over the ocean, seen in its coupled version (Voldoire et al., 2014). Compared to CNRM-CM5, an almost fully revised physical package has been developed and introduced in CNRM-CM6-1 (Abdel-Lathif et al., 2018). In particular, CNRM-CM6-1 has now a new scheme for the turbulence, which includes the cloud-top entrainment parameterization of Grenier and Bretherton (2001). Several of these developments are expected to influence the representation of stratocumulus, and needs to be assessed in detail.

We first describe the model characteristics in section 2, with a detailed description of both the turbulence and cloud schemes. Then, the data sets used in the model analysis are introduced in section 3. The low-cloud climatology, the stratocumulus annual cycle, and the associated CNRM-CM6-1 biases are documented for an AMIP simulation in section 4. The rest of the paper uses the Transpose-AMIP approach. Section 5 analyzes the drift of the model stratocumulus, to assess the usefulness of the framework and the time scales associated with the low-cloud errors. Finally, process-oriented sensitivity tests are performed to provide insight in the physical origins of the CNRM-CM6-1 stratocumulus biases, in particular to better disentangle whether they are associated to errors in the cloud parameterization input parameters or to structural errors of the parameterization itself (section 6). Section 7 summarizes the main findings of the present study and emphasizes some prospects to improve the representation of stratocumulus in the CNRM climate model

2. The CNRM-CM6-1 Climate Model

2.1. Overview

In this study, we use the atmospheric component of the CNRM climate model version 6 (CNRM-CM6-1 ARPEGE-Climat version 6.3 Its horizontal resolution corresponds to T127 spectral truncature (approximately 1.4° at the Equator). It has 91 vertical levels extending from the surface to about 80 km, 17 of them being within the marine boundary layer, below about 2 km. The model time step is 15 min. This new version mostly differs from that used in CNRM-CM5 (Voldoire et al., 2013), by an almost fully revisited atmospheric and surface physics. The turbulence and cloud schemes are detailed in the next section. The microphysics scheme is based on the work of Lopez (2002) and prognostically describes the mass fractions of cloud liquid and ice water, rainfall, and snow. The new convective scheme follows a mass-flux approach and aims at representing dry, shallow, and deep convection in a continuous way (Guérémy, 2011). The convective scheme's closure is based on a CAPE decaying equation with a relaxation time scale proportional to the time needed by a buoyant parcel to travel from the base to the top of the convective cloud. The convective microphysics is fully consistent with the large-scale microphysics, following the ideas of Piriou et al. (2007): it describes the same set of microphysical condensates. Entrainment and detrainment of the convective and large-scale condensates are taken into account. The longwave radiation scheme is based on the Rapid Radiation Transfer Model (Mlawer et al., 1997), issued from the cycle 37 of the ECMWF model. The shortwave component was developed by Fouquart and Bonnel (1980) and corresponds to the 6-band shortwave scheme used in the cycle 28r3 (https://www.ecmwf.int/en/elibrary/9198-part-iv-physical-processes) of the ECMWF model (Morcrette, 1991). Both the longwave and shortwave schemes are called every hour. The calculation of surface properties and surface fluxes is externalized via the SURFEX version 8 model (Masson et al., 2012). Over ocean, turbulent fluxes are computed using the ECUME iterative bulk parameterization (Belamari & Pirani, 2007). This parameterization is based on an optimization of neutral exchange coefficients under a wide variety of conditions, using measurements from several field campaigns.

2.2. The CNRM-CM6-1 Turbulence and Cloud Schemes

The CNRM-CM6-1 boundary-layer scheme describes the time evolution of the TKE with a 1.5-order prognostic equation (Cuxart et al., 2000). It is coupled to the cloud scheme following Ricard and Royer (1993; see below). The scheme makes use of the conservative variables of Betts (1973), that is the total cloud water q_t and the liquid potential temperature θ_l. The first-order turbulent fluxes of these variables (generically noted

ψ) are written in terms of their grid-scale vertical gradients and an eddy diffusivity coefficient K_ψ defined by Redelsperger and Sommeria (1981) and Cuxart et al. (2000):

$$\overline{\omega'\psi'} = -K_\psi \frac{\partial \overline{\psi}}{\partial z} \quad \text{, with} \quad K_\psi = C_\psi L_m \sqrt{e}\phi_3, \tag{1}$$

with C_ψ a tunable constant, L_m the mixing length defined in Bougeault and Lacarrère (1989), e the TKE, and ϕ_3 a stability function which allow to enhance turbulent mixing in unstable conditions and to reduce it in stable conditions (Cuxart et al., 2000).

An entrainment eddy diffusivity coefficient K_{inv} has been introduced to mimic PBL-top turbulence induced by vertical entrainment. This entrainment coefficient links subgrid turbulent fluxes of buoyancy to the mean buoyancy jump at the height of inversion (z_{inv}). Following the assumptions of Grenier and Bretherton (2001), this coefficient is defined as

$$K_{inv} = A_{inv} \frac{e_{inv}^{\frac{3}{2}}}{L_{inv} N_{inv}^2}, \tag{2}$$

where L_{inv}, e_{inv}, and N_{inv} are the PBL-top entrainment mixing length, TKE, and the Brunt-Väisälä frequency at the inversion, respectively. The nondimensional tunable coefficient A_{inv} is empirically defined to reproduce the observed sharp weakening of PBL-top entrainment. A_{inv} depends on the cloud-top inversion strength to capture that PBL-top entrainment strengthens moving from stratocumulus to shallow cumulus regimes (e.g., Kawa & Pearson Jr. 1989). This eddy diffusivity coefficient K_{inv} is only computed at the height of the inversion defined as the first model layer from the surface where the TKE is lower than a minimal threshold e_{min} (here $e_{min} = 0.01$ m^2/s^2). At this model level, the turbulence coefficient K is then taken as the maximum between the eddy diffusivity coefficient K_ψ and the entrainment coefficient K_{inv}. Over subtropical regions, the entrainment coefficient is active more than 95% of the time (not shown).

The cloud scheme is based on a statistical joint distribution of q_t and θ_l following the paradigm originally defined by Sommeria and Deardorff (1977) and modified by Bougeault (1981) and Ricard and Royer (1993). Assuming that the subgrid fluctuations of q_t and θ_l are weak, the treatment can be simplified using a unique variable s, which quantifies the distance to saturation in the q_t-θ_l space (Mellor, 1977). s is thus equivalent to a local saturation deficit, generalized to account for θ_l fluctuations. s reads:

$$s = \frac{a}{2}(q_t' - \alpha_1 \theta_l'), \tag{3}$$

$$\text{with} \quad a = \left[1 + \frac{L_v}{C_p}\left(\frac{\partial q_{sat}}{\partial T}\right)_{T=T_l}\right]^{-1} \tag{4}$$

$$\text{and} \quad \alpha_1 = \frac{T}{\theta}\left(\frac{\partial q_{sat}}{\partial T}\right)_{T=T_l}, \tag{5}$$

where primes indicate departure from the grid-scale variables, L_v is the latent heat of vaporization at 0 °C, C_p is the specific heat at constant pressure, q_{sat} is the saturated specific humidity, and T_l is the liquid temperature. This generalized saturation deficit is then normalized by its variance σ_s:

$$t = \frac{s}{\sigma_s} \tag{6}$$

$$\text{with} \quad \sigma_s = \frac{a}{2}\left[\overline{(q_t')^2} - 2\alpha_1 \overline{(q_t'\theta_l')} + (\alpha_1)^2 \overline{(\theta_l')^2}\right]^{1/2}. \tag{7}$$

From Cuxart et al. (2000), the second-order fluxes $\overline{(q_t')^2}$, $\overline{(q_t'\theta_l')}$, and $\overline{(\theta_l')^2}$ are related to the mixing length L_m, the temperature eddy diffusivity coefficient K_T (as defined in equation (1)) and the TKE. This leads to the parameterized turbulence variance :

$$\sigma_s = \frac{a}{2}\frac{1}{C}\sqrt{\frac{L_m K_T}{\sqrt{e}}}\left|\frac{\partial \overline{q_t}}{\partial z} - \alpha_1 \frac{\partial \overline{\theta_l}}{\partial z}\right| \tag{8}$$

$$\text{with} \quad \frac{1}{C} = 0.833. \tag{9}$$

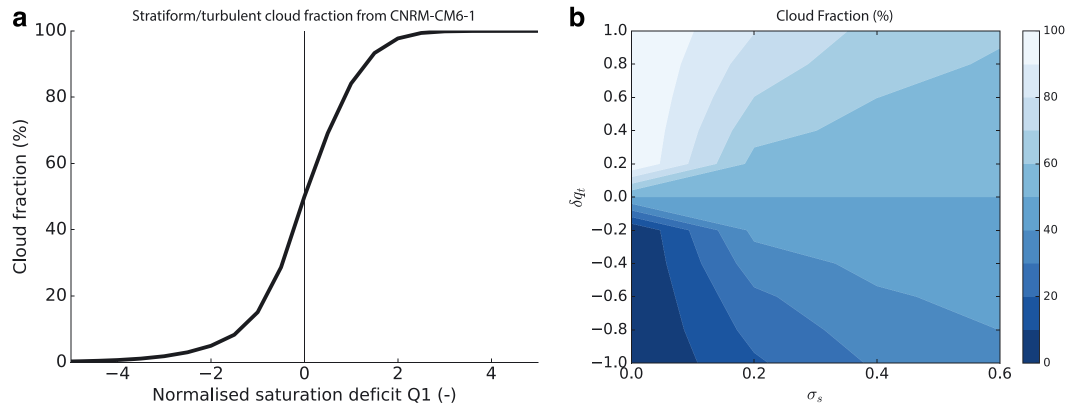

Figure 1. (a) Relationship between the normalized saturation deficit Q_1 and the large-scale cloud fraction as parameterized in the CNRM-CM6-1 model. (b) Parameterized cloud fraction (%) as a function of the turbulence variance (σ_s) and the saturation deficit $\overline{\delta q_t}$ for a = 0.35 (see equations (11) and (12)). CNRM = Centre National de Recherches Météorologiques.

Typical values for σ_s range between 0.08 and 0.2 g/kg for in situ measurements within stratocumulus and shallow cumulus, respectively (Wood et al., 2002).

The cloud fraction is then defined as the saturated part of the distribution of t:

$$\overline{CF} = \int_{-Q_1}^{+\infty} G(t)dt, \tag{10}$$

$$\text{where} \quad Q_1 = a\left[\frac{\overline{\delta q_t}}{2\sigma_s}\right] \tag{11}$$

$$\text{and} \quad \overline{\delta q_t} = \overline{q_t} - q_{sat}(\overline{T_l}). \tag{12}$$

G is assumed to follow a mix between a symmetric (Gaussian) and an asymmetric (exponential) probability distribution function (Bechtold et al., 1995; Bougeault, 1981). Figure 1a shows the precomputed relationship between Q_1 and cloud fraction used in the CNRM model. The sensitivity of the simulated cloud fraction to the internal variables of Q_1, that is, to the subgrid variability σ_s (equation (7)) and the saturation deficit $\overline{\delta q_t}$ (equation (12)) is further highlighted on Figure 1b. The value of a ranges from 0.32 to 0.42 in subsiding regions, in relation with changes in temperature and liquid water content profiles. To illustrate the sensitivity of the cloudiness to the other parameters, a is fixed to 0.35 (the overall behavior does not depend much on a). Figure 1b shows that a cloud fraction larger than 50% only occurs for oversaturated grid boxes ($Q_1 > 0$) and increases with decreasing standard deviation σ_s (i.e., increasing K_T or L_m or decreasing e—equation (8)). If the grid box is unsaturated ($Q_1 < 0$), cloud fraction remains lower than 50% and decreases with decreasing turbulence.

2.3. Model Configurations

Two configurations of the CNRM model are used in the present analysis. The first one consists in an AMIP configuration, in which the sea surface temperatures (SSTs) and sea ice cover are prescribed from the observations (Gates, 1992). This simulation covers the period from 1979 to 2016. The second configuration is based on a series of short-term initialized hindcasts following the Transpose-AMIP framework (Williams et al., 2013).

In the Transpose-AMIP configuration, the model is initialized every day at 00:00 UTC over the period covering 1–30 August 2013, leading to an ensemble of 30 hindcasts. Each hindcast is run over 30 days. The initial states (horizontal wind, surface pressure, temperature, specific humidity) come from the ERA-Interim reanalysis (Dee et al., 2011). Other model prognostic variables (in particular microphysics variables) are crudely initialized to zero, which may induce a spin-up of the model. The observed SSTs and sea ice cover are provided by the NCEP Optimally Interpolated weekly SST and Sea Ice data sets (Kanamitsu et al., 2002) and remain constant over the 30 days of each hindcast. Land surface conditions are initialized from an offline simulation of the SURFEX scheme forced by ERA-Interim data, for which surface precipitation has been rescaled so that their monthly mean equals the equivalent monthly mean of GPCC (Boisserie et al., 2016). Finally, note that aerosol concentrations are from the same data set as in the AMIP simulations, but remain constant across all the hindcasts (values from August 2013).

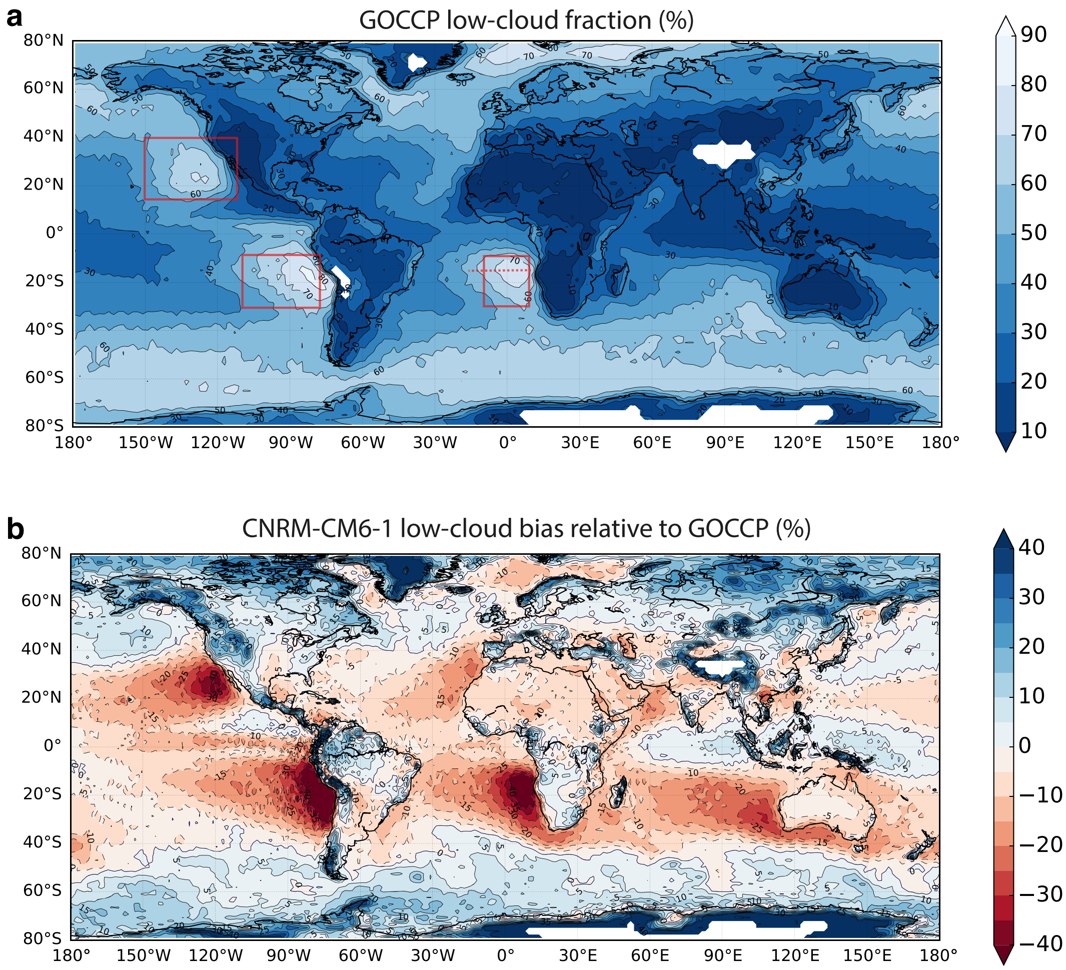

Figure 2. (a) Observed GOCCP annual-mean low-cloud fraction (%). (b) Low-cloud bias of the CNRM-CM6-1 AMIP simulation relative to the GOCCP climatology (%). Data are averaged between 2007 and 2015. Red boxes represent the three major stratocumulus regions used in the present study and the red dashed line indicates the South-East Atlantic low-cloud transect used in Figure 3. GOCCP = GCM Oriented CALIPSO Cloud Product; CNRM = Centre National de Recherches Météorologiques; AMIP =Atmospheric Model Intercomparison Project.

The hindcast period is defined such that the corresponding cloud biases of the reference AMIP simulation are representative of its climatological biases. Besides, August and September are chosen as cloud biases in the regions of interest are maximum during this season (see section 4.3). The period also allows to use space-based active measurements from the Lidar onboard the CALIPSO satellite (section 4.2) and the radiosoundings from the MAGIC field campaign (Lewis et al., 2012, see also Appendix A).

3. Reference Data Sets

ERA-Interim is used to characterize atmospheric conditions such as temperature and humidity (Dee et al., 2011). As a reference for clouds, we use the GCM Oriented CALIPSO Cloud Product (GOCCP) data set (Chepfer et al., 2010) based on measurements from the active sensor onboard the CALIPSO satellite (Winker et al., 2010). Vertical profiles of clouds are provided along its track, twice a day at a given location. The GOCCP product adjusts the raw data to allow direct comparison with climate models. Monthly and daily vertical profiles of cloud cover and horizontal distributions of low clouds (cloud-top pressure greater than 680 hPa) from January 2007 to December 2015, on a 2° × 2° horizontal grid, are used in the following. The use of a simulator would provide a more consistent comparison between model and observations (Klein & Jakob, 1999). However, on the one hand, simulators also have large uncertainties, in particular due to high-cloud attenuation and, on the other hand, given the large model biases, we expect our results to be rather insensitive to the use of a simulator. ERA-Interim cloud fraction and liquid water content will also be used, keeping in mind that this remains model variables. Hereafter, the analysis is performed on the CNRM model 1.4° × 1.4° horizontal grid,

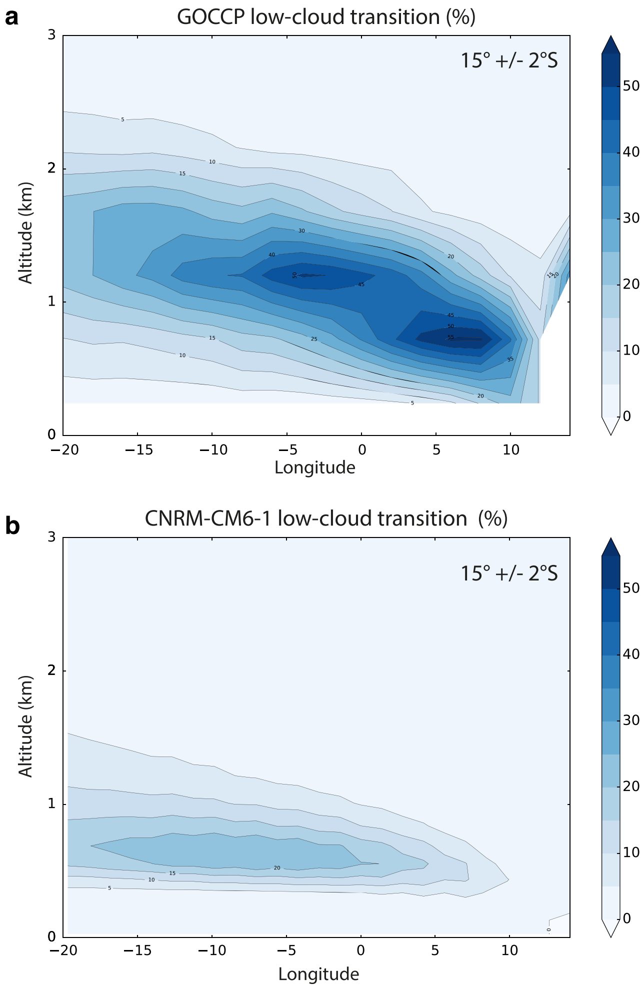

Figure 3. Zonal transition of the cloud vertical profile (%) averaged over a narrow meridional band (15 ± 2°S—Figure 2) in the South-East Atlantic ocean for (a) observations (as provided by GOCCP) and (b) the CNRM-CM6-1 AMIP model. Data are averaged between 2007 and 2015. GOCCP = GCM Oriented CALIPSO Cloud Product; CNRM = Centre National de Recherches Météorologiques; AMIP = Atmospheric Model Intercomparison Project.

using a bilinear interpolation for ERA-Interim and GOCCP data sets. The results are not sensitive to the choice of this grid. Note that no vertical interpolation has been performed.

4. Stratocumulus Clouds in the CNRM Model

4.1. Climatology

The model and observed climatologies are computed over the 9-year period from 2007 to 2015. GOCCP observations indicate that large low-cloud cover prevails mostly over the eastern parts of subtropical oceans and in the midlatitudes of both hemispheres (Figure 2a). In the following, we focus on subtropical areas where the largest cloud fractions (reaching 70–80%) are found and referred to as stratocumulus decks. The CNRM-CM6-1 AMIP simulation has fractions lower than 20% along the coast and lower than 30% offshore, leading to negative biases larger than 40% (Figure 2b). Regions of maximum low-cloud fractions are located further west than the observed one, suggesting that the model misses most of the stratus and stratocumulus regimes. As a result, shortwave cloud radiative effects, which, to the first order, scales with the low-cloud fraction in these regimes, are strongly underestimated and yield a large overestimation of the incoming solar radiation at the surface (not shown). The low-cloud spatial pattern of the CNRM-CM6-1 coupled simulations is very similar to their AMIP counterpart, albeit the biases are globally amplified (not shown). Thereafter, our analysis mostly focuses on the southeastern Atlantic region, which is one of the most biased region in low cloudiness.

4.2. Stratocumulus to Shallow Cumulus Cloud Transition

Figure 3a shows the zonal transition of the cloud vertical profiles observed over the southeastern Atlantic ocean (15 ± 2°S). The observed cloud fraction reduces from 50% near the coast to less than 25% offshore (westward to 10°W). The level of maximum cloudiness rises from 0.8 km to around 1.5 km, as moving away from the coast. The cloud base also elevates westward, following the deepening of the boundary layer. The CNRM-CM6-1 cloud fraction increases from less than 5% near the coast to 20% over the open ocean, between 10 and 5°W (Figure 3b). The boundary layer only slightly deepens westward. The model thus does not capture well the low-cloud transition. It misses a large part of stratus and stratocumulus clouds and simulates a too shallow boundary layer on average.

4.3. Annual Cycle

Figure 4a shows the annual cycle of the southeastern Atlantic low-cloud transect, computed over the 2007–2015 period. The GOCCP observations indicate that low-cloud fractions maximize around 5°E from August to October with values up to 90%. This maximum is explained by the northward migration of the Intertropical Convergence Zone that enhances the south hemisphere large-scale subsidence over the area, where it favors low-cloud formation and maintenance (Adam et al., 2017; Mechoso et al., 1995). The CNRM-CM6-1 atmospheric model exhibits a different annual cycle, maximizing low-cloud fractions further west (between 10 and 5°W) in December and January (Figure 4b). Finally, the region of weak low-cloud amount close to the coast expands much westward in the model. The low-cloud fraction bias is the largest in August and September, reaching errors up to 70%. In the following, the analysis focuses only on these 2 months.

4.4. Consistency Across Subsiding Regions

In situ data in the subtropical Atlantic are sparse. Using observations in regions with similar cloud regimes can be useful to evaluate more in depth the model errors. To assess to what extent cloud regimes and properties are similar across stratocumulus regimes, we identify three main regions of marine stratocumulus : the South-East Atlantic, the North-East Pacific, and the South-East Pacific (Figure 2a). Cloud biases simulated by the CNRM-CM6-1 atmospheric model over these areas are rather similar (Figure 2b). To get rid of regional

10.1029/2018MS001461

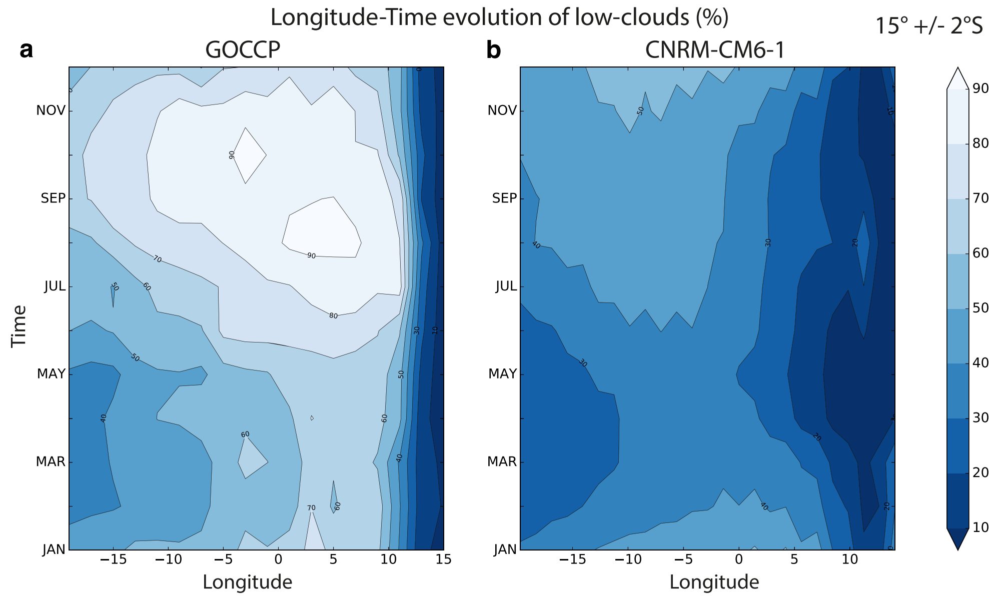

Figure 4. Longitude-Time evolution of low-cloud cover (%) along the South-East Atlantic zonal transect (15 ± 2°S—Figure 2) for (a) observations (GOCCP) and (b) the CNRM-CM6-1 AMIP simulation Data are averaged between 2007 and 2015. GOCCP = GCM Oriented CALIPSO Cloud Product; CNRM = Centre National de Recherches Météorologiques; AMIP= Atmospheric Model Intercomparison Project.

specificities, we relate low-cloud cover to the index of Klein and Hartmann (1993), characterizing the strength of the inversion at the top of the PBL.

This low-tropospheric stability (LTS) index is defined as the difference between the potential temperature at 700 hPa and at 1,000 hPa (Klein & Hartmann, 1993; Wood & Bretherton, 2006). It includes the adjustment of the free troposphere above the low clouds to deep convection in remote areas, through the propagation of gravity waves (e.g., Qu et al., 2015). As a consequence of these adjustments (which heats the free troposphere) and of the low SSTs, the eastern parts of ocean basins exhibit the highest LTS values (Figure 5). The CNRM-CM6-1 AMIP simulation captures quite well the LTS spatial pattern, albeit with a systematic underestimation of the LTS by about −3.0 K (Figure 5b), slightly stronger near the coasts. As the model is forced by observed SSTs, it emphasizes a significant cold bias of the tropical free troposphere, possibly associated with a deficit of convective heating in the Intertropical Convergence Zone.

The relationship between low-cloud cover and LTS provides an assessment of the ability of the model to simulate realistic cloud fractions for given large-scale conditions (as monitored by the LTS) and how the associated processes change from low LTS (shallow cumulus) to large LTS (stratocumulus and stratus) values. This relationship is determined for each of the three regions, using August-only daily mean fields over the 2007–2015 period. As a reference, we combine the GOCCP low-cloud cover and the ERA-Interim LTS, interpolated onto the coarser GOCCP 2° × 2° horizontal grid. Model data are also interpolated onto the same grid. The three regions of marine low-cloud transition are defined as: the South-East Atlantic (10–30°S, 10°W–10°E), the South-East Pacific (10–30°S, 80–110°W) and the North-East Pacific (15–40°N, 110–150°W). For each of these three regions, low-cloud cover is composited in LTS 1 K bins, ranging from 12 to 28 K.

Figure 6a shows the mean relationship between low-cloud fraction and LTS with uncertainties estimated as one interannual standard deviation (shading around each line). Observations show a rather linear increase of the low-cloud fraction with the boundary-layer stratification (∼+4% K^{-1}), reaching fraction up to 90% for LTS above 23 K (black lines on Figure 6a). This relationship is in agreement with previous studies (e.g., Klein & Hartmann, 1993; Sun et al., 2011). It is remarkably consistent across the three regions, except for low LTS values where cloud cover is weaker over the Northern Pacific than over the other regions. The model fails in capturing the observed mean slope. Cloud fraction is rather independent of LTS, near 35% from 15 to 21 K and

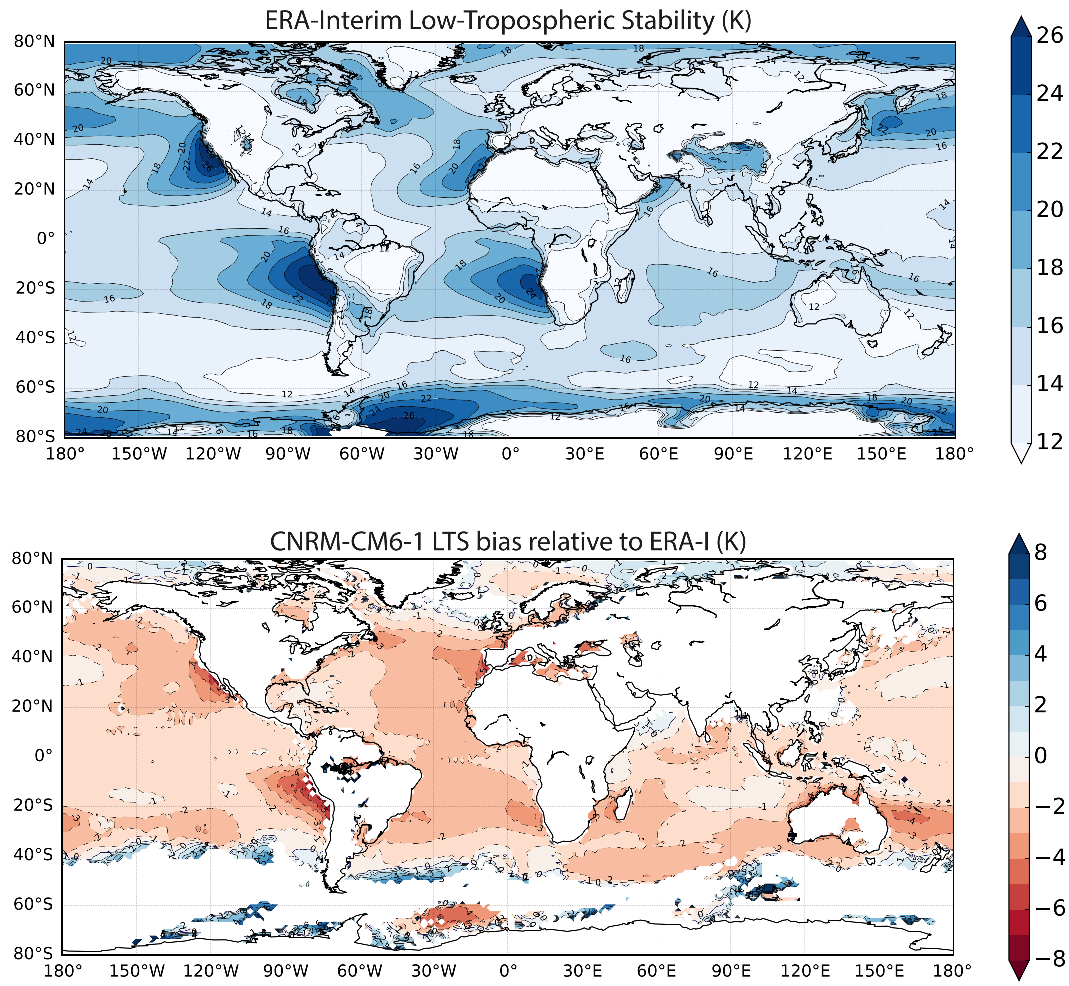

Figure 5. (a) LTS (in K) for August months averaged between 2007 and 2015 as given by ERA-Interim reanalysis. (b) LTS bias of the CNRM-CM6-1 AMIP simulation relative to the ERA-Interim climatology. Data are averaged between 2007 and 2015. CNRM = Centre National de Recherches Météorologiques; LTS = low-tropospheric stability.

then slightly decreases up to almost 20% near 24 K (red lines on Figure 6a). The model relationships between cloud fraction and LTS are also fully consistent across the three selected regions.

Figure 6b shows the LTS distributions of the reanalysis and the model. The reanalysis distribution strongly depends on the ocean basin. These differences mostly explain the cloud fraction differences between the three stratocumulus decks (e.g., higher in the South-East Atlantic, lower in North-East Pacific), as the relationship between the cloud fraction and the LTS remains mostly independent of the region considered (Figure 6a). The model captures to some extent these regional differences, although its distributions are systematically shifted toward lower LTS values by about 3–4 K, consistently with the systematic LTS underestimate mentioned earlier. Given that the model cloud fraction-LTS relationship does not depend on the region, the model average low-cloud fraction remains mostly constant across the three regions, with average fraction of about 32%.

These results suggests that the basic mechanisms underlying the subtropical marine low-cloud transitions are similar across the three basins. It implies that (1) the physical interpretation of model biases in a given low-cloud transition region is of relevance to what happens in other transition regions and (2) observed measurements in one low-cloud transition region are relevant to evaluate the model behavior in the context of these transitions. Besides, it also suggests that the model cloud biases are likely to be independent of the large-scale dynamics to the first order. The analysis of realistically initialized hindcasts will help us to

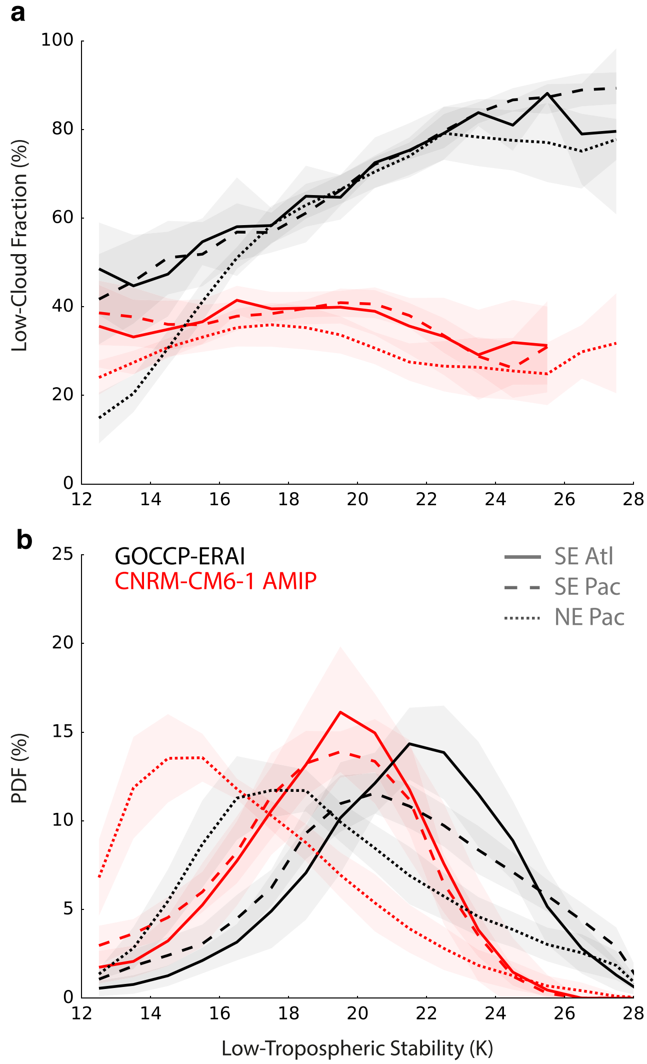

Figure 6. (a) Low-cloud fraction as a function of LTS (in K) and (b) PDF (in %) for the three major marine low-cloud regions. Black and red lines and shades represent time average and standard deviation over August months between 2007 and 2015 for observations (ERA-Interim + GOCCP) and the CNRM-CM6-1 AMIP simulation respectively. Full, dashed, and dotted lines represent the South Atlantic, South Pacific, and North Pacific regions, respectively (see Figure 2). GOCCP = GCM Oriented CALIPSO Cloud Product; CNRM = Centre National de Recherches Météorologiques; AMIP = Atmospheric Model Intercomparison Project; PDF = Probability Density Function; LTS = Low Tropospheric Stability.

characterize how these cloud biases settle and to further disentangle the role of the large-scale dynamical and thermodynamical conditions versus that of the local processes (i.e., the model parameterizations).

5. Stratocumulus Clouds in Short-Term Hindcasts

To analyze the setup of low-cloud biases, we conduct a 30-member ensemble of short-term hindcasts for August 2013 (section 2.3). The 30 members are averaged according to the lead time on a daily basis to assess the model drift from realistic initial conditions to its climatology. The ensemble mean is thus compared to monthly mean observations and AMIP outputs. Figure 7 shows the evolution of the low-cloud bias spatial pattern for 1-, 5-, and 30-day lead times. The daily GOCCP data set is used as a reference for clouds. For a given Day-N lead time, the observation reference is obtained as the average over the 30 days starting from August Nth (e.g., the 5-day lead-time reference spans 5 August to 3 September). After 1 day, large negative biases already exist over the whole tropical area, with maximum over the eastern part of the subtropical oceans. After 5 days, the low-cloud bias slightly reduces in the trade-wind regions, but remains strongly negative in stratocumulus regions. This is related to the longer adjustment of the liquid water content (~2 days) in shallow

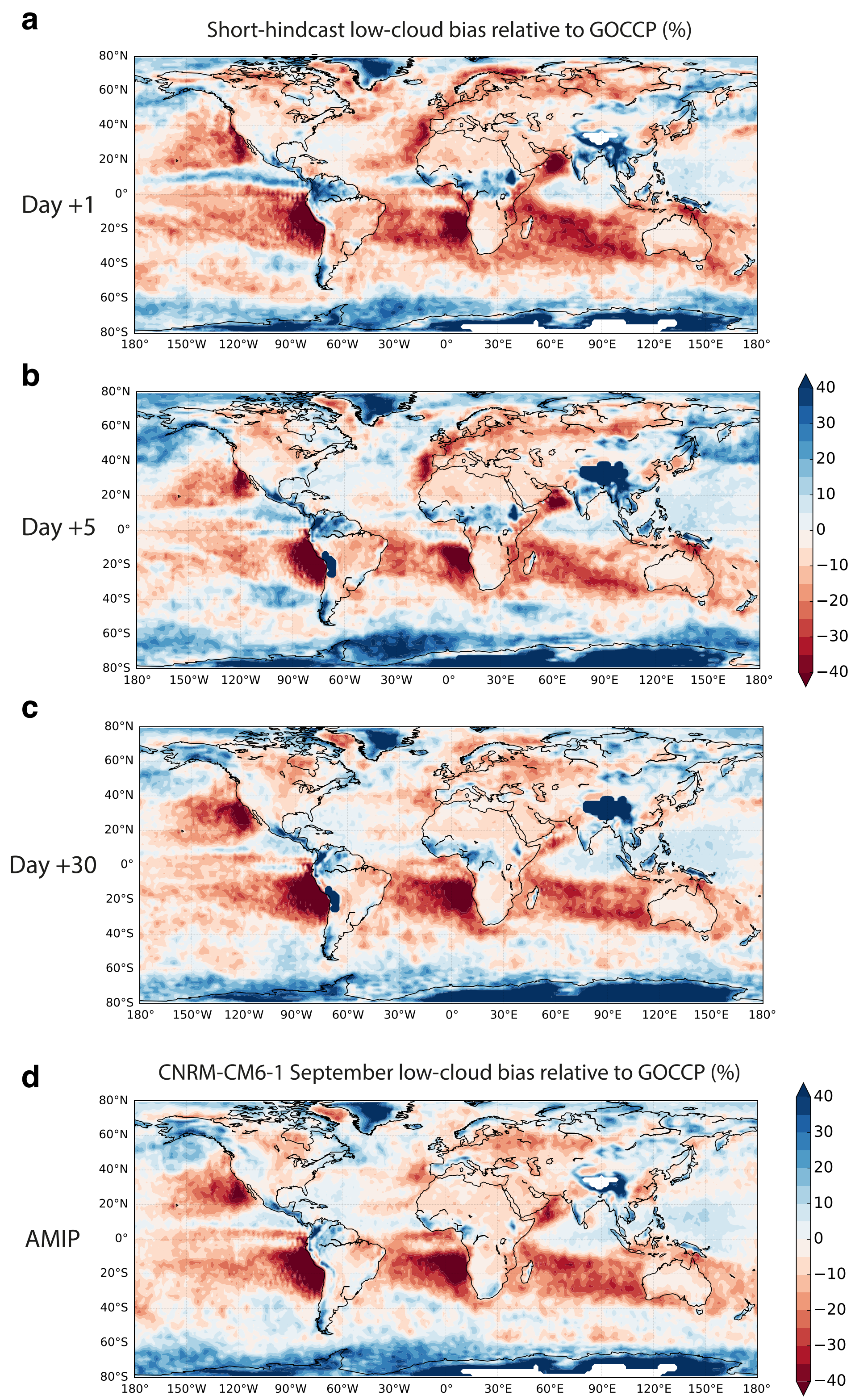

Figure 7. Evolution of spatial pattern of biases in low-cloud cover (%) for 1- (a), 5- (b), and 30-day (c) lead times averaged over the 30 members of the short-term hindcast ensemble. The last row represents the climatological bias averaged using the CNRM-CM6-1 AMIP simulation (d). Biases are computed relative to observations (GOCCP) averaged over the 30 days starting from August Nth for the Day-N lead time (e.g., the 5-day lead time GOCCP reference spans 3 August to 3 September). Observations are also averaged over the years 2007-2015. GOCCP = GCM Oriented CALIPSO Cloud Product; CNRM = Centre National de Recherches Météorologiques; AMIP = Atmospheric Model Intercomparison Project.

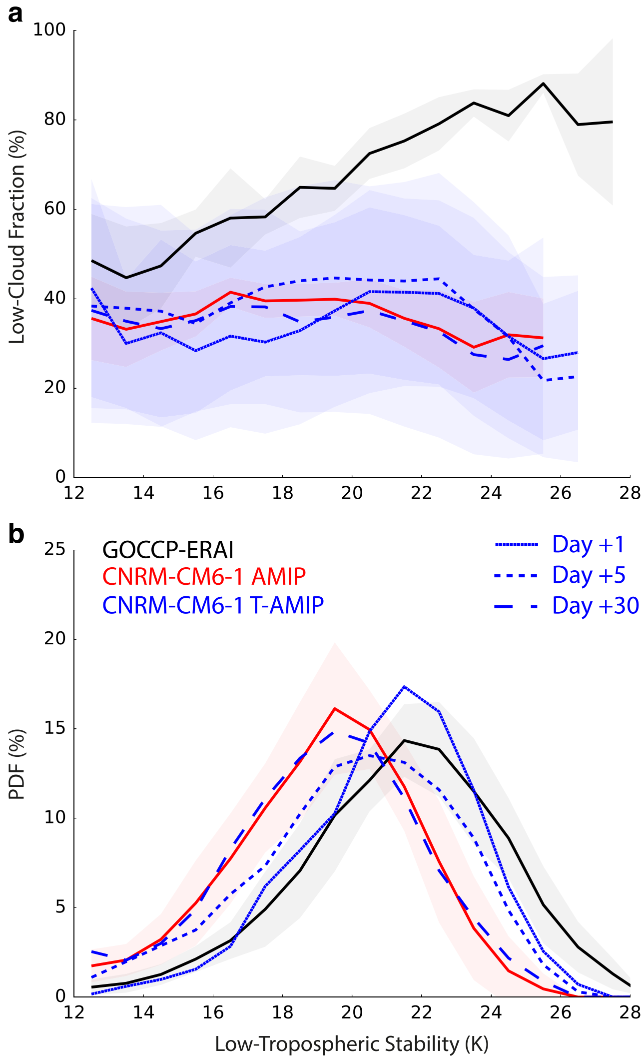

Figure 8. (a) and (b) as Figure 6a and 6b, respectively, for the South Atlantic region only (Figure 2). The 30-member ensemble of short-term hindcasts are represented as full, dotted, and dashed blue lines averaged for 1-, 5-, and 30-day lead time, respectively. Black and red lines correspond to observed and model distributions for climatological August between 2007 and 2015 (as seen on Figure 6). GOCCP = GCM Oriented CALIPSO Cloud Product; CNRM = Centre National de Recherches Météorologiques; AMIP = Atmospheric Model Intercomparison Project; T-AMIP = Transpose-AMIP; PDF = Probability Density Function.

cumulus regions. The spatial pattern of the low-cloud bias is rather similar for longer lead times (Figure 7c), suggesting that most of the climatological low-cloud biases are reached in about 5 days. Finally, the low-cloud bias spatial pattern after 30 days lead time is also very similar to the climatological spatial pattern (Figure 7d).

Figure 8a shows the low-cloud fraction as a function of LTS over the southeastern Atlantic region for different lead times. It is compared to the relationship found in the AMIP simulation and in the observation (see also Figure 6a). The hindcast ensemble shows an approximately constant low-cloud fraction (~35%) for most LTS values. This relationship does not depend much on the lead time. It is remarkably similar to that in the AMIP simulation, although the low-cloud fraction is slightly higher for the largest LTS (~+5%). Figure 8b shows the LTS distribution for the same lead times. As expected, the model LTS distribution resembles the reanalysis distribution at 1-day lead time. The model LTS distribution then evolves slowly toward its AMIP climatology. The large-scale dynamics drift thus involves processes slower than those of the low clouds. This also confirms that the CNRM-CM6-1 low-cloud biases are to the first order independent of the large-scale biases.

The Transpose-AMIP framework is relevant to further understand the origins of the CNRM-CM6-1 low-cloud biases. Given that Transpose-AMIP simulations at short lead times (~1 day) already exhibit low-cloud biases despite realistic temperature and humidity profiles (see Appendix A for a validation of the hindcast states using the MAGIC radiosoundings), we focus hereafter on the 24-hr lead time of the hindcast ensemble to address this question. Note that the spin-up in the regions of our interest is only a few hours (not shown).

6. Process-Oriented Analysis of the Low-Cloud Bias

6.1. Low-Cloud Decomposition in Relative Humidity

The LTS distribution has been shown reasonable during the first days of the Transpose-AMIP hindcasts. The LTS index however characterizes mainly the larger scales of the atmosphere, while the origin of the cloud cover underestimate is probably more local. Indeed, the CNRM-CM6-1 stratiform cloud fraction is a function of one predictor Q_1, defined as the ratio between the grid-scale saturation deficit and its subgrid variability (section 2 and Figure 1). Q_1 involves four variables (Appendix B): the grid-box averaged relative humidity *RH*, temperature *T* and liquid water content q_l, and the standard deviation σ_s of *s*, which is related to the strength of turbulence. The sensitivity of the cloud parameterization to these four input parameters is investigated. Therefore, in the following, we focus on the relationship between the maximum cloud fraction below 3 km (*CF*) and its associated relative humidity (*RH*), which explains the *CF* variability to the first order. Note also that the spatial and temporal variability of *CF* within the southeastern Atlantic region is highly correlated with that of the low-cloud cover, as used hereabove (correlation around 0.96).

The cloud fraction *CF* is stratified according to *RH*, so as to compare the link between *RH* and cloud fraction in the model, in the ERA-Interim reanalysis and between the reanalyzed *RH* and GOCCP *CF*. We focus here on the southeastern Atlantic region. From the 30-member Transpose-AMIP ensemble, the maximum cloud fraction is computed using instantaneous fields of cloud profiles at the first time step and at 24-hr lead time (i.e., 00 UTC). For ERA-Interim, we also use instantaneous fields at 00 UTC. For GOCCP, we use the nighttime daily data set, as it is very close to 00 UTC over the South-East Atlantic. The domain-average maximum cloud fraction $\overline{CF}$ thus reads

$$\overline{CF} = \sum_i P_i\, CF_i \quad \text{with } i \text{ as } RH \text{ bins.} \tag{13}$$

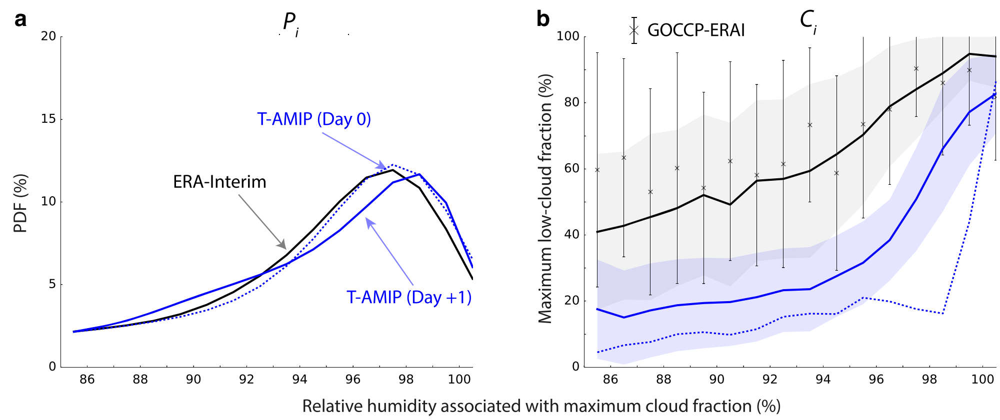

Figure 9. (a) PDF of the relative humidity *RH* associated with the maximum cloud fraction below 3 km *CF*. (b) Composite of the cloud amount *CF* as a function of *RH*. ERA-Interim reanalysis on August 2013 at 00 UTC is represented as a black line, the short-term hindcast ensemble at initialization as a dashed blue line and at 1-day lead time as a solid blue line. Here short-term hindcasts *CF* at 0 lead time is computed using ERA-Interim initial states during the first time step. *CF* uncertainties (shade) used ±1 standard deviation of *CF* within each bin. Maximum observed cloud fraction (GOCCP) is also plotted against ERA-Interim *RH* as black crosses and vertical lines for mean values and standard deviation (within bin values), respectively. PDF = Probability Density Function; T-AMIP = Transpose-Atmospheric Model Intercomparison Project; GOCCP = GCM Oriented CALIPSO Cloud Product.

CF_i refers to the mean value of *CF* in the dynamical regime *i* defined by *RH* and P_i the frequency of occurrence of the *i*th bin of *RH*.

Figure 9 shows the components of equation (13), namely, the *RH* distribution (P_i) and the composite cloud fraction *CF* as a function of *RH* (CF_i). ERA-Interim *RH* distribution is negatively skewed, the highest frequency of occurrence being for *RH* ∼97% (Figure 9a). The low-level cloud fraction increases with relative humidity (∼+6% per percent for *RH* between 91% and 99%—Figure 9b). The relationship between the GOCCP maximum cloud fraction *CF* and the ERA-Interim *RH* (black dots) also indicates an increase of *CF* with *RH*. GOCCP and ERA-Interim cloud distribution are very consistent with each other. It suggests that ERA-interim accurately represents maximum values of low-cloud fraction.

By construction, the CNRM-CM6-1 hindcast initial *RH* distribution is close to that of ERA-Interim (dashed blue line on Figure 9a). At the first time step, simulated cloud fraction is around 20% when *RH* is lower than 98% and is high only over almost-saturated grid cells (Figure 9b). After 24 hr (solid blue lines), the *RH* distribution maximum has shifted toward higher values relative to the reanalysis distribution. The model overestimates the frequency of occurrence of low *RH* values below 93% and underestimates that of moderate *RH* values between 93% and 98%. The *RH* distribution remains unchanged for lead time up to 5 days (not shown). The composite cloud fraction CF_i has increased in all *RH* bins, suggesting a cloud fraction dependence on *RH* similar to that in ERA-Interim below 96%. For the highest *RH* values, the model cloud fraction sharply increases reaching cloud fractions close to observations and ERA-Interim. Overall, the model has a negative offset of about 30%. The relationship between *CF* and *RH* is markedly altered during the first day and remains unchanged for longer lead times (not shown). This is probably due to the crude initialization of the liquid water content and subgrid variability to zero. Their relative role will be discussed in the next section.

6.2. Sensitivity of Clouds to Errors in Input Parameters

The relative influence of the cloud parameterization input parameters on the *CF*-*RH* relationship is estimated using offline calculations of the averaged cloud fraction within each *RH* bin. Using 1-day lead-time outputs, we use bin-averaged hindcast parameters (i.e., T, q_l, σ_s) to calculate the cloud fraction, following equation (B4) (Appendix B). The *CF*-*RH* relationship obtained with these offline calculations is roughly similar to that diagnosed directly from the hindcast outputs (purple dashed line with squares on Figure 10b) in the range 93–98%. *CF* is underestimated outside this range of *RH*. Nevertheless, this offline approach seems relevant to quantify the *CF* sensitivity to input parameters.

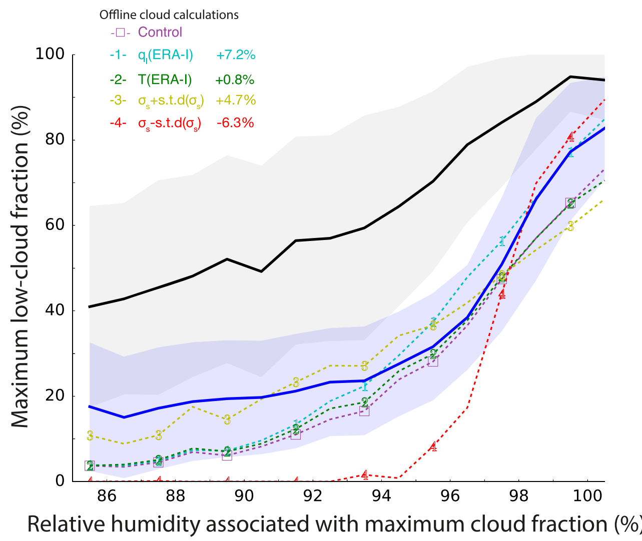

Figure 10. As Figure 9b for ERA-Interim (black line) and CNRM-CM6-1 (blue line) along with various sensitivity tests to cloud parameterization input parameters. Reference offline computations of cloud fraction (equation (B4)) using bin-averaged input parameters from hindcasts after 1-day lead time are plotted as purple squared dotted lines. Sensitivity tests to ERA-Interim liquid water content (cyan), temperature (green), or to the strength of σ_s (by adding [yellow] or subtracting [red] one standard deviation [s.t.d.] of σ_s to its grid-mean value σ_s) are plotted as dotted lines. Numbers correspond to domain-average change of cloud fraction relative to Control weighted by the 1-day lead time *RH* distribution for each sensitivity test.

Several sensitivity tests are thus performed:

1. The role of the liquid water content is addressed using the values from ERA-Interim (Note that the CNRM-CM6-1 cloud parameterization is implemented such that the input liquid water is that obtained at the end of the previous time step, which thus was impacted by both model microphysics and advection. Thus, no a priori consistency between this input liquid water and other input parameters of the parameterization is expected in the model). The resulting *CF-RH* relationship shows an increase of *CF* for *RH* greater than 94% (cyan dashed lines on Figure 10) but *CF* still remains significantly underestimated. Correcting the model liquid water underestimate contributes to reduce the domain-average low-cloud bias by 7% relative to the control calculation (mostly due to the moistest grid cells).
2. The role of temperature is then tackled, also using ERA-Interim. As the offline computations are done within each *RH* bin and thus imply to keep *RH* constant, the specific humidity is implicitely adjusted. As expected from the weak evolution of temperature within the first 24 hr of the hindcasts, the resulting *CF-RH* relationship is very close to the original offline calculation (green dashed lines on Figure 10).
3. The sensitivity to the subgrid standard deviation σ_s is crudely quantified by systematically adding or subtracting one standard deviation (s.t.d.) of σ_s to its grid-mean value. These two offline calculations (yellow and red dashed lines on Figure 10, respectively) mostly changes the steepness of the *CF-RH* relationship, yet not enough for compensating the general underestimate of low clouds. Note that the model turbulence strength σ_s is around 0.1 g/kg, which is consistent with observations within stratocumulus (Wood et al., 2002).

This analysis suggests that some improvements in the representation of low clouds by the CNRM model might be expected by improving the representation of its input parameters. However, the cloud bias sensitivity to these parameters remains small. Note that these offline calculations does not take into account the positive feedback between liquid water content and cloud fraction, which may enhance cloud cover independently of *RH* (Appendix B). Nevertheless, the results of this section call for a better understanding of how structural aspects of the cloud parameterization shape the model low clouds.

6.3. Impact of Two Turbulence-Cloud Parameterization Structural Choices on the Low-Cloud Bias

In the present section, we examine the impact of two structural choices associated with the turbulence-cloud parameterizations: the activation of the enhanced entrainment at the top of the PBL (equation (2)), and the

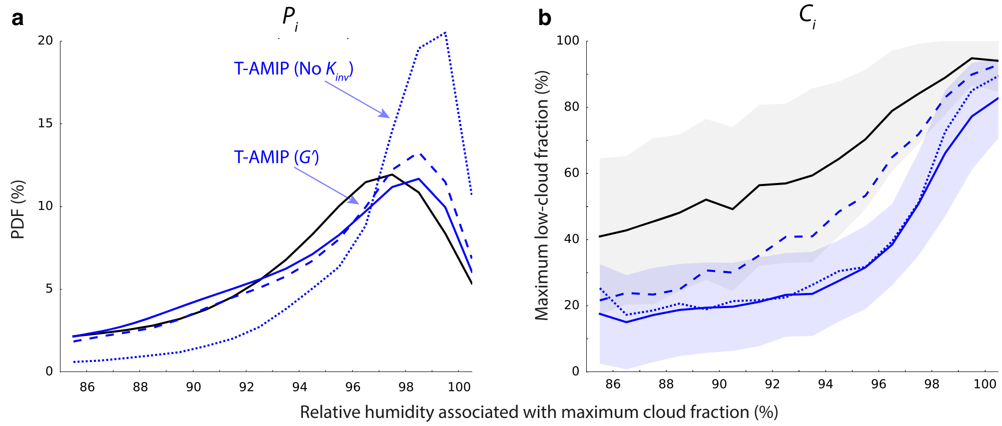

Figure 11. As Figure 9 but with only ERA-Interim (black) and the short-term hindcast ensemble at 1-day lead time (solid blue), to be compared to sensitivity tests with no cloud-top entrainment (dotted blue lines) and with modified subgrid distribution of cloud predictors (dashed blue lines). PDF = Probability Density Function; T-AMIP = Transpose-Atmospheric Model Intercomparison Project.

probability density function used to describe the subgrid distribution of s (equation (10)). The objective is here to assess whether these structural choices need to be revisited in the CNRM model in a near future.

A first sensitivity experiment is conducted by switching off the entrainment parameterization at the top of the PBL (i.e., no use of K_{inv}, see section 2.2). The *RH* distribution radically changes (Figure 11a): the dry PBL events are now not frequent enough, while the very moist PBL events ($RH > 97\%$) become overly frequent and promote the occurrence of large low-cloud fraction. In contrast, the *CF*-*RH* relationship remains almost unchanged with respect to the reference hindcasts (Figure 11b). As a result, the regional cloud fraction (Table 1) is increased, but at the expense of an error compensation, with a strongly unrealistic *RH* distribution. The PBL-top entrainment thus does not play much on the *CF*-*RH* relationship, but this process significantly controls the *RH* distribution, at least in the CNRM-CM6-1 model. A better calibration of its parameterization might help to improve the *RH* distribution realism.

The role of the chosen subgrid distribution of s is now addressed. The paradigm of Bougeault (1981) supposed that the cloud fraction is a simple, precomputed function of Q_1 (equation (10) and Figure 1a). Several studies have suggested that the saturation deficit subgrid-scale distribution exhibits a significant asymmetry, often associated with different modes. In the case of cumulus clouds, this asymmetry has been argued to describe both the region impacted by shallow convective updrafts, and its environment, using either

Table 1
Decomposition of the Average Bias (ΔCF) of Maximum Cloud Fraction Below 3 km (CF in %) Over the Southeastern Atlantic Region

	$\overline{\Delta CF}$	$\sum CF_i \Delta P_i$	$\sum P_i \Delta CF_i$	$\sum \Delta P_i \Delta CF_i$
AMIP	−39	−3.3	−37	1.3
T-AMIP (Day 0)	−49	1.1	−50	0.1
T-AMIP (Day +1)	−30	0.1	−31	0.8
T-AMIP (Day +5)	−33	1.7	−35	0.2
T-AMIP (No K_{inv})	−13	9.8	−28	5.6
T-AMIP (G')	−11	2.0	−14	0.9

Note. The mean cloud bias in the CNRM-CM6-1 model with respect to the reanalysis is decomposed in contributions related to biases in the *RH* distribution (ΔP_i), structural cloud biases (ΔC_i), and the covariance between them (see equation (14)). For the AMIP simulations, values have been averaged over August 2013. For the control hindcast ensemble (Transpose-AMIP), errors are indicated at initialization (Day 0), and for 1- and 5-day lead times (Day +1 and Day +5). Two sensitivity tests applied in the hindcast ensemble are also listed for 1-day lead time: without PBL-top entrainment (No K_{inv}) and with a modified subgrid distribution of cloud predictors (G'). AMIP = Atmospheric Model Intercomparison Project; T-AMIP = Transpose-AMIP.

large-eddy simulations (e.g., Jam et al., 2013; Neggers, 2009; Perraud et al., 2011) and or in situ observations (Wood & Field, 2000). This asymmetry remains unclear in the context of stratocumulus (Wood & Field, 2000). The combination of at least two subgrid-scale distributions has been shown to improve the representation of low clouds in atmospheric models (Larson et al., 2002). The statistical moments of the updraft distribution are usually derived from the shallow convection scheme, while the moments of the environment distribution remain diagnosed from grid-scale properties. In a simple and crude attempt to mimic this bimodal distribution, we add to the original subgrid distribution a second Gaussian distribution. This latter is positioned such that its mean is +1 (0 for the environment distribution), to provide more favorable conditions for cloud formation. Furthermore, we assume that thermal characteristics influences the distribution of *s* over about 70% of the grid cell (the remaining 30% would correspond to the environment). This leads to a negatively skewed bi-Gaussian distribution and a new relationship between Q_1 and *CF* relative to the original distribution (Figure 1). A skewed distribution increases cloudiness when the saturation excess is weak but positive, which seems more consistent with observations (Wood & Field, 2000). The ratio between the two Gaussian distributions and the mean of the second one have been rather arbitrarily chosen to reveal the effect of the thermal distribution. A more physically based approach is of course needed. At the 1-day lead time, the *RH* distribution is slightly shifted toward higher *RH* values but remains rather similar to that in the reference hindcasts (Figure 11a). However, the *CF-RH* relationship is improved in all *RH* bins reducing the low-cloud underestimate by around 50% (Figure 11b). This crude test thus calls for a revisit of the cloud parameterization subgrid-scale distribution, and in particular to better account from other sources of moisture subgrid-scale variability.

6.4. Impact of Parameterization Structural Choices on the Regional Low-Cloud Biases

Using equation (13), we now quantify the impact of structural errors of the domain-mean cloud bias. This leads to the following decomposition:

$$\overline{\Delta CF} = \sum_i CF_i \Delta P_i + \sum_i P_i \Delta CF_i + \sum_i \Delta P_i \Delta CF_i, \tag{14}$$

where Δ indicates the difference between the model and the reanalysis. The first term in the right hand side quantifies the contribution of errors in the *RH* distribution to the domain-average cloud bias. The second term arises from biases in the *CF-RH* relationship. The last term corresponds to covariations between cloud and relative humidity errors and is generally smaller than the first two terms.

Table 1 summarizes these different terms for different configurations and experiments of the CNRM model. It confirms the large underestimate of low clouds in the southeastern Atlantic region in the AMIP simulation climatology (∼40%), as previously suggested in Figure 7d. This underestimate is mainly related to errors in the *CF-RH* relationship.

Low-cloud biases in the hindcast ensemble are large. They decrease with lead times (see Figure 7). As in the AMIP simulation, the domain-average cloud bias is largely related to errors in the sensitivity of *CF* to *RH* (Table 1 and Figure 9b). The domain-average cloud biases in sensitivity tests to parameterization structural choices are significantly reduced from −30% to around −12% relative to ERA-Interim cloud fraction (Table 1). However, this improvement is mostly related to amplified biases in *RH* distribution when the entrainment parameterization has been switched off (No K_{inv}), whereas it is related to improved sensitivity of *CF* to *RH* with modified subgrid distribution of cloud predictors (G').

7. Conclusions

In this study, we investigate the physical origins underlying the lack of low clouds over the eastern parts of tropical ocean basins simulated by the CNRM-CM6-1 model. In simulations forced by observed SST, this low-cloud bias can be larger than 40% in stratocumulus and stratus cloud regimes. Short-term hindcasts, initialized by ERA-Interim reanalyses and following the Transpose-AMIP framework (Williams et al., 2013), reproduce these climatological errors, so that they are useful to quantify the timescales associated with the low-cloud bias growth. The model reaches its climatological bias within about 5 days. Despite realistic temperature and humidity profiles in the hindcast initial state, the lack of stratocumulus appears after only a few time steps. This fast response of the low-cloud bias is attributable to the model physics and involves errors both in the input parameters of the cloud parameterization and in the turbulence-cloud parameterization itself. The large-scale dynamical adjustments are weak during the first few days.

Process-oriented sensitivity tests are conducted using this short-term hindcast framework, to further identify the low-cloud systematic error origin. The cloud underestimate in the CNRM-CM6-1 model is partly attributable to the cloud parameterization input variables, mostly through underestimation of liquid water content. This error influences cloud fraction by underestimating the saturation deficit, which is estimated with the liquid temperature. The cloud bias is also critically linked to turbulence and cloud parameterization. The deactivation of the parameterization of PBL-top entrainment increases cloud fractions, but at the cost of too moist marine PBLs. The cloud bias is reduced but for wrong reasons. On the contrary, modification of the subgrid-scale saturation deficit distribution is able to increase the low-cloud cover, while keeping similar boundary layers.

Our results thus suggest that the CNRM-CM6-1 turbulence-cloud parameterization requires improvements, at least in two ways:

1. The parameterization of PBL-top entrainment originally described in Grenier and Bretherton (2001) needs to be revised to improve the distribution of the relative humidity in the stratocumulus boundary layer. A better calibration of the parameterization is likely to be needed. Numerical artifacts might also be involved, such as the difficulty to define a robust criterion to detect the PBL top or to represent large inversion strengths for current vertical resolutions (Bretherton et al., 2004; Bretherton & Park, 2009).
2. The cloud scheme should better represent the subgrid-scale variability of temperature and humidity, and especially should account for boundary-layer features that organizes it, such as updrafts and downdrafts. For instance, a number of studies have highlighted the importance of using bimodal distributions to characterize and reproduce boundary-layer clouds (Jam et al., 2013; Neggers, 2009; Wood & Field, 2000). Following this idea, the CNRM-CM6-1 convection scheme can provide relevant information (updraft area fraction, temperature, and moisture) that may be used to modify the subgrid turbulence assumptions (e.g., Qin et al., 2018). Note also that the paradigm of Bougeault (1981) was originally developed for trade-wind cumulus layers, and there is a need to assess which distribution law is most appropriate for stratocumulus cloud layers.

Input variables to the cloud parameterization have also been found to impact the cloud fraction, but to a lesser extent than a few structural choices in the turbulence-cloud parameterization. In particular, the subgrid-scale variance of the saturation deficit σ_s^2 requires further investigations using for instance observations (Wood et al., 2002) and large-eddy simulations of stratocumulus (e.g., Duynkerke et al., 2004). Such simulations will also be useful to better constrain or revise the PBL-top entrainment parameterization in CNRM-CM6-1.

From a more methodological point of view, our study confirms that the use of short-term hindcasts with a climate model (i.e., the Transpose-AMIP framework) provides a powerful approach to investigate root causes of atmospheric biases, as already emphasized in previous studies (Ma et al., 2014; Medeiros et al., 2012; Zheng et al., 2017). On the one hand, it allows to disentangle processes that have different timescales (e.g., boundary-layer processes versus the large-scale dynamics). On the other hand, it nicely complements more traditional ways used to develop and test parameterizations (e.g., SCMs): it provides a testbed for these parameterizations over a wide set of atmospheric conditions, while keeping the computational cost reasonable.

Appendix A: Assessment of ERA-Interim and CNRM-CM6-1 Boundary-Layer Inversions in the North-Eastern Pacific

The goal of this appendix is twofold : (1) assessing the realism of the Transpose-AMIP framework in the very first step of the hindcasts and (2) evaluating vertical profiles of cloud fraction simulated by the CNRM-CM6-1 model to both ERA-Interim and space-based observation profiles. This evaluation reinforce our trust in the hindcast framework and guide us for building sensitivity tests described in the main text.

Boundary-layer characteristics in ERA-Interim and in CNRM-CM6-1 short-term hindcasts are assessed using sounding measurements, which provide high-resolution vertical profiles of humidity and temperature. Only a few campaigns provide a significant number of measurements in marine stratocumulus regions. One of them is the Marine Atmospheric Radiation Measurement (ARM) GEWEX/WGNE Pacific Cross-section Intercomparison (GPCI) Investigation of Clouds (MAGIC) campaign that took place from October 2012 to September 2013 (Lewis et al., 2012) over the northeastern Pacific region. The consistency across subtropical stratocumulus regions highlighted in section 4.4 suggests that the conclusions that can be derived for this region are very likely relevant for other stratocumulus regions. Sixty balloon-borne soundings are available during August

10.1029/2018MS001461

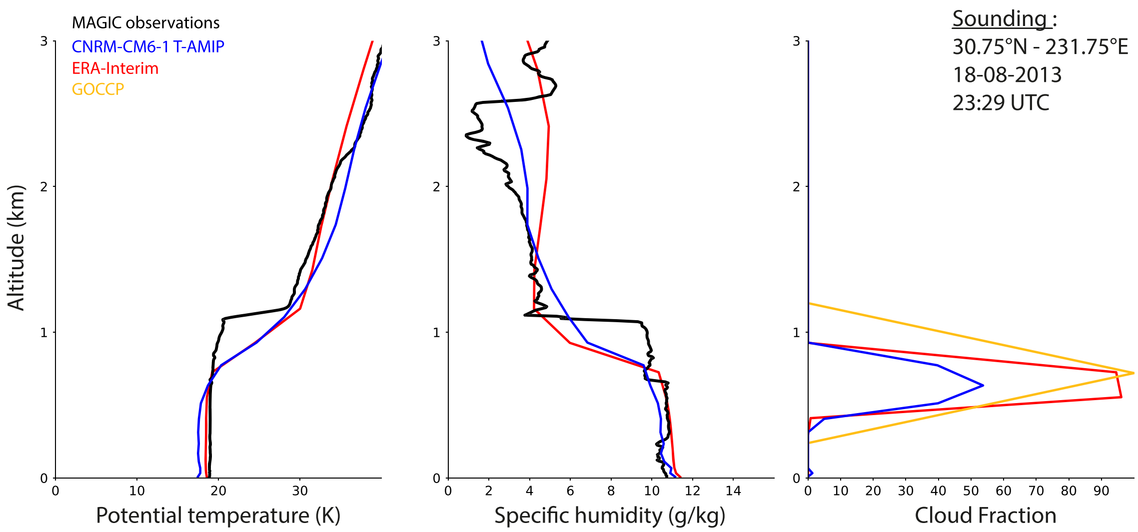

Figure A1. Vertical profiles of potential temperature, specific humidity, and cloud fraction. Temperature and humidity profiles arise from a specific balloon-borne sounding launched during the MAGIC campaign (located 30.75°N–231.75°E, at 23:29 UTC on 18 August 2013) with the closest cloud profile from the GOCCP day-night data set. Red and blue profiles correspond to ERA-Interim and the short-term hindcast ensemble taken as being the closest point in time and space to the sounding, using native horizontal and vertical resolution and 4X daily outputs. MAGIC = Marine ARM GPCI Investigation of Clouds; T-AMIP = Transpose-Atmospheric Model Intercomparison Project; CNRM = Centre National de Recherches Météorologiques; GOCCP = GCM Oriented CALIPSO Cloud Product.

2013 and inside the North-East Pacific region (15–40°N, 110–150°W—see Figure 2). The soundings are collocated with ERA-Interim and CNRM-CM6-1 short-term hindcasts using the nearest grid point and the closest time instant (using 6-hourly output) to each of these radiosoundings. An example for potential temperature and specific humidity profiles is shown on Figures A1a and A1b. Native vertical resolutions is used for each data set. Reanalysis and model heights of the boundary-layer and inversion strengths are in agreement with each other (as expected from the initialization by ERA-Interim). However, the sharpness and the height of the boundary-layer top are underestimated relative to the sounding measurement. This misrepresentation is seen in a majority of locations within the defined region. The too weak inversion strength may be related to the coarser vertical resolution in models.

To evaluate models more robustly, inversion strengths and altitudes are further characterized. The ERA-Interm reanalysis and observed humidity and temperature profiles are interpolated on the CNRM vertical levels. Then we detect the maximum vertical gradient of either potential temperature or specific humidity and its altitude, which are supposed to define the inversion strength and altitude, respectively. Their bidimensional probability density distributions are finally computed on and shown on Figure A2. This figure confirms that the boundary-layer height decreases in accordance with the inversion strength. Model vertical gradients of potential temperature are often too strong, for shallower PBL. The moisture inversion distributions are more consistent across the three data sets. Note, however, that the vertical interpolation significantly weakens inversion strengths in the sounding data set. This confirms that boundary-layer characteristics in ERA-Interim, and thus for hindcast initialization, are rather realistic *when interpolated on the same coarse vertical grid*.

Figure A1c also shows the cloud profile for ERA-Interim and the CNRM-CM6-1 corresponding hindcast. The nearest GOCCP cloud profile from the sounding is also plotted. ERA-Interim is able to reproduce the right location and amount of low clouds at this location, explaining the consistency among data set seen on Figure 9b. On the contrary, CNRM-CM6-1 simulates the right altitude of cloud fraction maximum but underestimates it by 50%.

Appendix B: Offline Calculation of Cloud Fraction

Offline calculation of the cloud fraction is powerful to assess its sensitivity to the cloud parameterization input parameters. In the CNRM-CM6-1 model, stratiform cloud fraction is related to the Q_1 variable, which is the ratio between $\overline{\delta q_t}$ and σ_s (equation (7)). While the latter is calculated by the model turbulence scheme, the former is linked to grid-scale averaged thermodynamical fields. The saturation deficit $\overline{\delta q_t}$ is defined as $\overline{q_t} - q_s(\overline{T_l}, \overline{P})$

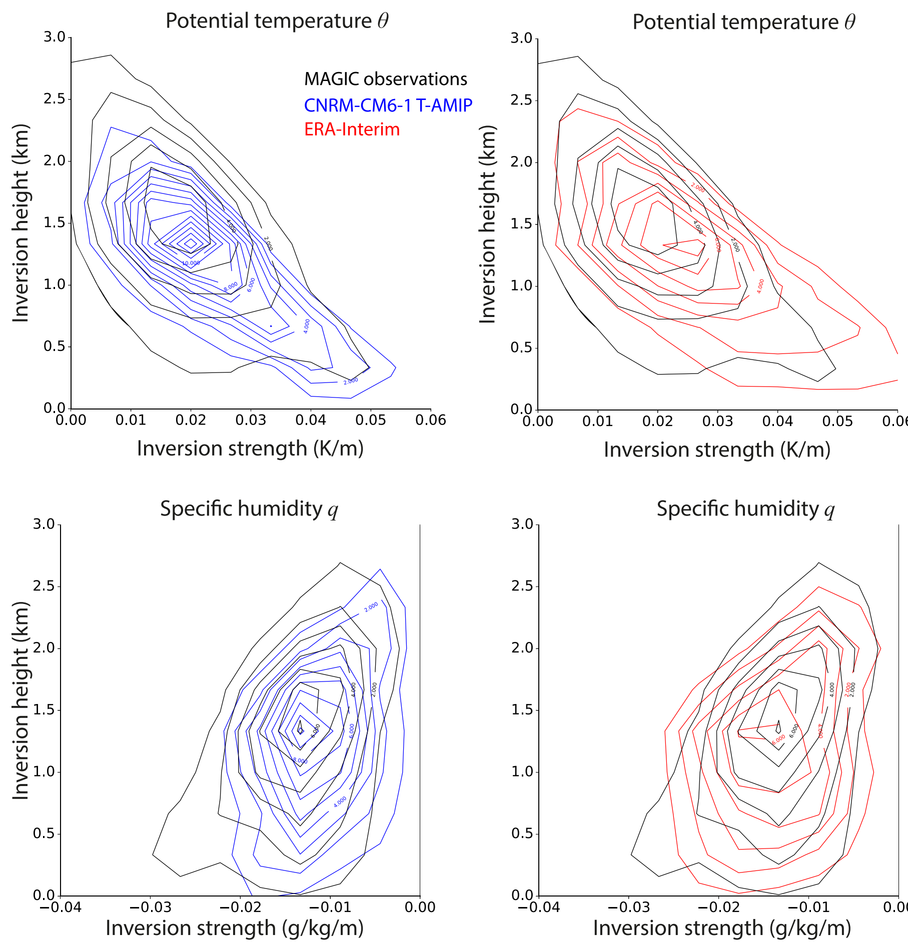

Figure A2. Mean altitude-strength probability density functions. Instantaneous outputs of ERA-Interim (red) and short-term hindcast (blue) outputs over the north-east Pacific region are used. Height and strength of inversion are defined as the altitude where lies the maximum vertical gradient of (top) potential temperature and (bottom) specific humidity below 3 km. The black distribution are based on the 60 sounding measurements launched during the MAGIC campaign during August 2013 inside the north-east pacific region (15–40°N, 110–150°W). Data are extracted at 00 UTC for ERA-Interim and for 1-day lead time for the short-term hindcast ensemble. Before computation, ERA-Interim data have been interpolated on the CNRM-CM6-1 horizontal grid and each of both selected ERA-Interim output and sounding measurements have been interpolated vertically on the CNRM-CM6-1 vertical levels. MAGIC = Marine ARM GPCI Investigation of Clouds; CNRM = Centre National de Recherches Météorologiques; T-AMIP = Transpose-Atmospheric Model Intercomparison Project.

with

$$\overline{q_t} = \overline{RH}\, q_s(\overline{T}, \overline{P}) + \overline{q_l}, \tag{B1}$$

$$\overline{T_l} = \overline{T} - \frac{L}{c_p}\overline{q_l}. \tag{B2}$$

$\overline{RH}$ and $\overline{q_l}$ are the grid-scale relative humidity and liquid water content, respectively. With the assumption that second-order terms can be neglected (Bougeault, 1981), one can simplify the liquid water saturation specific humidity:

$$q_s(\overline{T_l}, \overline{P}) = q_s(\overline{T}, \overline{P}) \left[1 + \frac{L}{R_v \overline{T_l}^2}(\overline{T} - \overline{T_l})\right]^{-1}. \tag{B3}$$

Using equations (B1), (B2), and (B3), the $\overline{\delta q_t}$ difference can be rewritten as:

$$\overline{\delta q_t} = (\overline{RH} - \epsilon) \cdot q_s(\overline{T}, \overline{P}) + \overline{q_l}, \tag{B4}$$

with

$$\epsilon = \frac{1}{1 + \frac{L^2 \overline{q_l}}{R_v c_p (\overline{T} - \frac{L}{c_p} \overline{q_l})^2}}. \tag{B5}$$

In the case without condensate ($\overline{q_l} = 0$, $\epsilon = 1$), equation (B4) is reduced to the more classic saturation deficit and the cloud fraction is simply a function of relative humidity and temperature. For a given relative humidity value, $\overline{\delta q_t}$ increases with condensates ($\overline{q_l}>0$). Since $\overline{\delta q_t}$ is linearly related to Q_1 and cloud fraction (equation (11)), this suggests that cloud condensates help cloud maintenance.

Equation (B4) can be used to calculate Q_1 (equation (11)) and cloud fraction (equation (10)), knowing grid-scale values of $\overline{RH}$, $\overline{T}$, $\overline{P}$, $\overline{q_l}$, and σ_s. The sensitivity of cloud fraction to each of these variables can then be quantified (section 6.2).

Acknowledgments
The research leading to these results received funding from the EU FP7/2007-2013 under grant agreement 603521, project PREFACE. We acknowledge support from Agence Nationale de la Recherche (ANR) (grant HIGH-TUNE #ANR-16-CE01-0010). We also acknowledge the work performed by the CNRM climate model development team, which developed the physical package used in the present study. We thank two anonymous reviewers and Peter Caldwell for their insightful comments on the manuscript and thank Fleur Couvreux for useful discussions. This work was supported by the DEPHY2 project, funded by the French national program LEFE/INSU. ERA-Interim reanalysis and CALIPSO-GOCCP observations were downloaded on the ECMWF website (http://apps.ecmwf.int/datasets/) and from the CFMIP-Observation website (http://climserv.ipsl.polytechnique.fr/cfmip-obs/Calipso_goccp.html), respectively. We thank the MAGIC team for providing observations downloaded from the ARM website (http://www.archive.arm.gov/discovery/). The CNRM-CM6 model outputs are available on request to R.R. (romain.roehrig@meteo.fr).

References

Abdel-Lathif,A. Y., Roehrig,R., Beau,I., & Douville,H. (2018).Single-column modeling of convection during the CINDY2011/DYNAMO field campaign with the CNRM climate model version 6.*Journal of Advances in Modeling Earth Systems*, *10*, 578–602. https://doi.org/10.1002/2017MS001077

Adam, O., Schneider, T., & Brient, F. (2017). Regional and seasonal variations of the double-ITCZ bias in CMIP5 models. *Climate Dynamics*, *51*, 1–17.

Ahlgrimm, M., Forbes, R. M., Hogan, R. J., & Sandu, I. (2018). Understanding global model systematic shortwave radiation errors in sub-tropical marine boundary layer cloud regimes. *Journal of Advances in Modeling Earth Systems*, *10*, 2042–2060. https://doi.org/10.1029/2018MS001346

Bechtold, P., Cuijpers, J., Mascart, P., & Trouilhet, P. (1995). Modeling of trade wind cumuli with a low-order turbulence model: Toward a unified description of Cu and Se clouds in meteorological models. *Journal of the Atmospheric Sciences*, *52*(4), 455–463.

Belamari, S., & Pirani, A. (2007). Validation of the optimal heat and momentum fluxes using the ORCA2-LIM global ocean-ice model. (MERSEA Integrated Project, Tech. Rep., 88 pp.).

Betts, A. (1973). Non-precipitating cumulus convection and its parameterization. *Quarterly Journal of the Royal Meteorological Society*, *99*(419), 178–196.

Betts, A., & Miller, M. (1986). A new convective adjustment scheme. Part II: Single column tests using GATE wave, BOMEX, ATEX and arctic air-mass data sets. *Quarterly Journal of the Royal Meteorological Society*, *112*(473), 693–709.

Bony, S., & Dufresne, J.-L. (2005). Marine boundary layer clouds at the heart of tropical cloud feedback uncertainties in climate models. *Geophysical Research Letters*, *32*, L20806. https://doi.org/10.1029/2005GL023851

Boisserie, M., Decharme, B., Descamps, L., & Arbogast, P. (2016). Land surface initialization strategy for a global reforecast dataset. *Quarterly Journal of the Royal Meteorological Society*, *142*, 880–888. https://doi.org/10.1002/qj.2688

Bougeault, P. (1981). Modeling the trade-wind cumulus boundary layer. Part I: Testing the ensemble cloud relations against numerical data. *Journal of the Atmospheric Sciences*, *38*, 2414–2428.

Bougeault, P., & Lacarrère, P. (1989). Parameterization of orography-induced turbulence in a mesobeta–scale model. *Monthly Weather Review*, *117*(8), 1872–1890.

Bretherton, C.-S., Ferrari, R., & Legg, S. (2004). Climate process teams: A new approach to improving climate models. *U.S. CLIVAR Variations Newsletter*, *2*(1), 1–6.

Bretherton, C. S., & Park, S. (2009). A new moist turbulence parameterization in the community atmosphere model. *Journal of Climate*, *22*(12), 3422–3448.

Bretherton, C. S., & Wyant, M. (1997). Moisture transport, lower-tropospheric stability, and decoupling of cloud-topped boundary layers. *Journal of the Atmospheric Sciences*, *54*(1), 148–167.

Brient, F., Schneider, T., Tan, Z., Bony, S., Qu, X., & Hall, A. (2016). Shallowness of tropical low clouds as a predictor of climate models' response to warming. *Climate Dynamics*, *47*, 1–17.

Caldwell, P., Bretherton, C. S., & Wood, R. (2005). Mixed-layer budget analysis of the diurnal cycle of entrainment in southeast pacific stratocumulus. *Journal of the Atmospheric Sciences*, *62*(10), 3775–3791.

Chen, T., Rossow, W. B., & Zhang, Y. (2000). Radiative effects of cloud-type variations. *Journal of Climate*, *13*(1), 264–286.

Chepfer, H., Bony, S., Winker, D., Cesana, G., Dufresne, J., Minnis, P., et al. (2010). The GCM-oriented CALIPSO cloud product (CALIPSO-GOCCP). *Journal of Geophysical Research*, *115*, D00H16. https://doi.org/10.1029/2009JD012251

Cuxart, J., Bougeault, P., & Redelsperger, J.-L. (2000). A turbulence scheme allowing for mesoscale and large-eddy simulations. *Quarterly Journal of the Royal Meteorological Society*, *126*(562), 1–30. https://doi.org/10.1002/qj.49712656202

Dal Gesso, S, Van der Dussen, J., Siebesma, A., De Roode, S., Boutle, I., Kamae, Y, et al. (2015). A single-column model intercomparison on the stratocumulus representation in present-day and future climate. *Journal of Advances in Modeling Earth Systems*, *7*, 617–647. https://doi.org/10.1002/2014MS000377

De Szoeke, S. P., Fairall, C. W., Wolfe, D. E., Bariteau, L., & Zuidema, P. (2010). Surface flux observations on the southeastern tropical Pacific Ocean and attribution of SST errors in coupled ocean–atmosphere models. *Journal of Climate*, *23*(15), 4152–4174.

De Szoeke, S. P., Yuter, S., Mechem, D., Fairall, C. W., Burleyson, C. D., & Zuidema, P. (2012). Observations of stratocumulus clouds and their effect on the eastern Pacific surface heat budget along 20 S. *Journal of Climate*, *25*(24), 8542–8567.

Dee, D., Uppala, S., Simmons, A., Berrisford, P., Poli, P., Kobayashi, S., et al. (2011). The ERA-Interim reanalysis: Configuration and performance of the data assimilation system. *Quarterly Journal of the Royal Meteorological Society*, *137*(656), 553–597.

Duynkerke, P. G., de Roode, S. R., van Zanten, M. C., Calvo, J., Cuxart, J., Cheinet, S., et al. (2004). Observations and numerical simulations of the diurnal cycle of the EUROCS stratocumulus case. *Quarterly Journal of the Royal Meteorological Society*, *130*(604), 3269–3296.

Fouquart, Y., & Bonnel, B. (1980). Computations of solar heating of the Earth's atmosphere- A new parameterization. *Beitrage zur Physik der Atmosphare*, *53*, 35–62.

Gates, W. L. (1992). AMIP: The atmospheric model intercomparison project. *Bulletin of the American Meteorological Society*, *73*(12), 1962–1970.

Grenier, H., & Bretherton, C. S. (2001). A moist PBL parameterization for large-scale models and its application to subtropical cloud-topped marine boundary layers. *Monthly Weather Review*, *129*(3), 357–377.

Guérémy, J. (2011). A continuous buoyancy based convection scheme: One-and three-dimensional validation. *Tellus A*, *63*(4), 687–706.

Hannay, C., Williamson, D. L., Hack, J. J., Kiehl, J. T., Olson, J. G., Klein, S. A., et al. (2009). Evaluation of forecasted southeast Pacific stratocumulus in the NCAR, GFDL, and ECMWF models. *Journal of Climate*, *22*(11), 2871–2889.

Hartmann, D. L., Ockert-Bell, M. E., & Michelsen, M. L. (1992). The effect of cloud type on Earth's energy balance: Global analysis. *Journal of Climate*, *5*, 1281–1304.

Hourdin, F., Găinuşă-Bogdan, A., Braconnot, P., Dufresne, J.-L., Traore, A.-K., & Rio, C. (2015). Air moisture control on ocean surface temperature, hidden key to the warm bias enigma. *Geophysical Research Letters*, *42*, 10,885–10,893. https://doi.org/10.1002/2015GL066764

Jam, A., Hourdin, F., Rio, C., & Couvreux, F. (2013). Resolved versus parametrized boundary-layer plumes. Part III: Derivation of a statistical scheme for cumulus clouds. *Boundary-Layer Meteorology*, *147*(3), 421–441.

Kanamitsu, M., Ebisuzaki, W., Woollen, J., Yang, S. K., Hnilo, J., Fiorino, M., & Potter, G. (2002). NCEP-DOE AMIP-II reanalysis (R-2). *Bulletin of the American Meteorological Society*, *83*(11), 1631–1644.

Kawa, S., & Pearson Jr., R (1989). An observational study of stratocumulus entrainment and thermodynamics. *Journal of the Atmospheric Sciences*, *46*(17), 2649–2661.

Klein, S. A., & Hartmann, D. L. (1993). The seasonal cycle of low stratiform clouds. *Journal of Climate*, *6*, 1587–1606.

Klein, S. A., & Jakob, C. (1999). Validation and sensitivities of frontal clouds simulated by the ECMWF model. *Monthly Weather Review*, *127*, 2514–2531.

Köhler, M, Ahlgrimm, M, & Beljaars, A (2011). Unified treatment of dry convective and stratocumulus-topped boundary layers in the ECMWF model. *Quarterly Journal of the Royal Meteorological Society*, *137*(654), 43–57.

Larson, V. E., Golaz, J.-C., & Cotton, W. R. (2002). Small-scale and mesoscale variability in cloudy boundary layers: Joint probability density functions. *Journal of the Atmospheric Sciences*, *59*(24), 3519–3539.

Lewis, E. R., Wiscombe, W. J., Albrecht, B. A., Bland, G. L., Flagg, C. N., Klein, S. A., et al. (2012). Magic: Marine ARM GPCI investigation of clouds. United States: DOE Office of Science Atmospheric Radiation Measurement (ARM) Program. https://www.arm.gov/publications/programdocs/doe-sc-arm-12-020.pdf?id=67

Lilly, D. K. (1968). Models of cloud-topped mixed layers under a strong inversion. *Quarterly Journal of the Royal Meteorological Society*, *94*(401), 292–309.

Lock, A. (1998). The parametrization of entrainment in cloudy boundary layers. *Quarterly Journal of the Royal Meteorological Society*, *124*(552), 2729–2753.

Lock, A. (2001). The numerical representation of entrainment in parameterizations of boundary layer turbulent mixing. *Monthly Weather Review*, *129*(5), 1148–1163.

Lock, A., Brown, A., Bush, M., Martin, G., & Smith, R. (2000). A new boundary layer mixing scheme. Part I: Scheme description and single-column model tests. *Monthly Weather Review*, *128*(9), 3187–3199.

Lopez, P. (2002). Implementation and validation of a new prognostic large-scale cloud and precipitation scheme for climate and data-assimilation purposes. *Quarterly Journal of the Royal Meteorological Society*, *128*(579), 229–257.

Ma, H.-Y., Xie, S., Klein, S., Williams, K., Boyle, J., Bony, S., et al. (2014). On the correspondence between mean forecast errors and climate errors in CMIP5 models. *Journal of Climate*, *27*(4), 1781–1798.

Martin, G., Ringer, M., Pope, V., Jones, A., Dearden, C., & Hinton, T. (2006). The physical properties of the atmosphere in the new Hadley Centre Global Environmental Model (HadGEM1). Part I: Model description and global climatology. *Journal of Climate*, *19*(7), 1274–1301.

Masson, V., Le Moigne, P., Martin, E., Faroux, S., Alias, A., Alkama, R., et al. (2012). The SURFEX v7.2 land and ocean surface platform for coupled or offline simulation of Earth surface variables and fluxes. *Geoscientific Model Development Discussions*, *5*, 3771–3851.

Mechoso, C. R., Robertson, A. W., Barth, N., Davey, M., Delecluse, P., Gent, P., et al. (1995). The seasonal cycle over the tropical pacific in coupled ocean–atmosphere general circulation models. *Monthly Weather Review*, *123*(9), 2825–2838.

Mechoso, C., Wood, R., Weller, R., Bretherton, C. S., Clarke, A., Coe, H., et al. (2014). Ocean–cloud–atmosphere–land interactions in the southeastern pacific: The vocals program. *Bulletin of the American Meteorological Society*, *95*(3), 357–375.

Medeiros, B., Williamson, D. L., Hannay, C., & Olson, J. G. (2012). Southeast pacific stratocumulus in the community atmosphere model. *Journal of Climate*, *25*(18), 6175–6192.

Mellado, J. P. (2017). Cloud-top entrainment in stratocumulus clouds. *Annual Review of Fluid Mechanics*, *49*, 145–169.

Mellor, G. L. (1977). The gaussian cloud model relations. *Journal of the Atmospheric Sciences*, *34*(2), 356–358.

Mlawer, E. J., Taubman, S. J., Brown, P. D., Iacono, M. J., & Clough, S. A. (1997). Radiative transfer for inhomogeneous atmospheres: RRTM, a validated correlated-k model for the longwave. *Journal of Geophysical Research*, *102*(D14), 16663–16.

Moeng, C.-H., & Stevens, B. (2000). Representing the stratocumulus-topped boundary layer in GCMs In D. A. Randall (Ed.), *General circulation model development: Past, present, and future* (pp. 577–604). Academic Press.

Morcrette, J. J. (1991). Radiation and cloud radiative properties in the European Centre for Medium Range Weather Forecasts forecasting system. *Journal of Geophysical Research*, *96*(D5), 9121–9132.

Morcrette, C. J., O'Connor, E. J., & Petch, J. C. (2012). Evaluation of two cloud parametrization schemes using ARM and Cloud-Net observations. *Quarterly Journal of the Royal Meteorological Society*, *138*(665), 964–979.

Nam, C., Bony, S., Dufresne, J. L., & Chepfer, H. (2012). The "too few, too bright" tropical low-cloud problem in CMIP5 models. *Geophysical Research Letters*, *39*, L21801. https://doi.org/10.1029/2012GL053421

Neggers, R. A. J. (2009). A dual mass flux framework for boundary layer convection. Part II: Clouds. *Journal of the Atmospheric Sciences*, *66*(6), 1489–1506.

Nicholls, S. (1984). The dynamics of stratocumulus: Aircraft observations and comparisons with a mixed layer model. *Quarterly Journal of the Royal Meteorological Society*, *110*(466), 783–820.

Nicholls, S. (1989). The structure of radiatively driven convection in stratocumulus. *Quarterly Journal of the Royal Meteorological Society*, *115*(487), 487–511.

Perraud, E., Couvreux, F., Malardel, S., Lac, C., Masson, V., & Thouron, O. (2011). Evaluation of statistical distributions for the parametrization of subgrid boundary-layer clouds. *Boundary-Layer Meteorology*, *140*(2), 263–294.

Phillips, T. J., Potter, G. L., Williamson, D. L., Cederwall, R. T., Boyle, J. S., Fiorino, M., et al. (2004). Evaluating parameterizations in general circulation models: Climate simulation meets weather prediction. *Bulletin of the American Meteorological Society*, *85*(12), 1903–1915.

Piriou, J.-M., Redelsperger, J.-L., Geleyn, J.-F., Lafore, J.-P., & Guichard, F. (2007). An approach for convective parameterization with memory: Separating microphysics and transport in grid-scale equations. *Journal of the Atmospheric Sciences*, *64*(11), 4127–4139.

Qin, Y., Lin, Y., Xu, S., Ma, H.-Y., & Xie, S. (2018). A diagnostic PDF cloud scheme to improve subtropical low clouds in NCAR community atmosphere model (CAM 5). *Journal of Advances in Modeling Earth Systems*, *10*, 320–341. https://doi.org/10.1002/2017MS001095

Qu, X., Hall, A., Klein, S. A., & Caldwell, P. M. (2015). The strength of the tropical inversion and its response to climate change in 18 CMIP5 models. *Climate Dynamics*, *45*(1-2), 375–396.

Randall, D. A., Xu, K.-M., Somerville, R. J., & Iacobellis, S. (1996). Single-column models and cloud ensemble models as links between observations and climate models. *Journal of Climate*, *9*(8), 1683–1697.

Redelsperger, J.-L., & Sommeria, G. (1981). Méthode de représentation de la turbulence d'échelle inférieure à la maille pour un modèle tri-dimensionnel de convection nuageuse. *Boundary-Layer Meteorology*, *21*(4), 509–530.

Ricard, J., & Royer, J. (1993). A statistical cloud scheme for use in an AGCM. *Annales Geophysicae*, *11*, 1095–1115.

Richter, I. (2015). Climate model biases in the eastern tropical oceans: Causes, impacts and ways forward. *Wiley Interdisciplinary Reviews: Climate Change*, *6*(3), 345–358.

Siebesma, A.-P., Bretherton, C. S., Brown, A., Chlond, A., Cuxart, J., Duynkerke, P. G., et al. (2003). A large eddy simulation intercomparison study of shallow cumulus convection. *Journal of the Atmospheric Sciences*, *60*(10), 1201–1219.

Siebesma, A. P., Soares, P. M., & Teixeira, J. (2007). A combined eddy-diffusivity mass-flux approach for the convective boundary layer. *Journal of the Atmospheric Sciences*, *64*(4), 1230–1248.

Sommeria, G., & Deardorff, J. (1977). Subgrid-scale condensation in models of nonprecipitating clouds. *Journal of the Atmospheric Sciences*, *34*(2), 344–355.

Sušelj, K., Teixeira, João, & Chung, D. (2013). A unified model for moist convective boundary layers based on a stochastic eddy-diffusivity/mass-flux parameterization. *Journal of the Atmospheric Sciences*, *70*(7), 1929–1953.

Sun, F., Hall, A., & Qu, X. (2011). On the relationship between low cloud variability and lower tropospheric stability in the southeast pacific. *Atmospheric Chemistry and Physics*, *11*(17), 9053–9065.

Tan, Z., Kaul, C. M., Pressel, K. G., Cohen, Y., Schneider, T., & Teixeira, J. (2018). An extended eddy-diffusivity mass-flux scheme for unified representation of subgrid-scale turbulence and convection. *Journal of Advances in Modeling Earth Systems*, *10*, 770–800. https://doi.org/10.1002/2017MS001162

Toniazzo, T., & Woolnough, S. (2014). Development of warm SST errors in the southern tropical Atlantic in CMIP5 decadal hindcasts. *Climate Dynamics*, *43*(11), 2889–2913.

Tsushima, Y., Ringer, M. A., Koshiro, T., Kawai, H., Roehrig, R., Cole, J., et al. (2016). Robustness, uncertainties, and emergent constraints in the radiative responses of stratocumulus cloud regimes to future warming. *Climate Dynamics*, *46*(9-10), 3025–3039.

Vannière, B., Guilyardi, E., Toniazzo, T., Madec, G., & Woolnough, S. (2014). A systematic approach to identify the sources of tropical SST errors in coupled models using the adjustment of initialised experiments. *Climate Dynamics*, *43*(7-8), 2261–2282.

Voldoire, A, Claudon, M, Caniaux, G, Giordani, H, & Roehrig, R (2014). Are atmospheric biases responsible for the tropical Atlantic SST biases in the CNRM-CM5 coupled model?. *Climate Dynamics*, *43*(11), 2963–2984.

Voldoire, A., Sanchez-Gomez, E., Salas y Mlia, D., Decharme, B., Cassou, C., Snsi, S., et al. (2013). The CNRM-CM5. 1 global climate model: Description and basic evaluation. *Climate Dynamics*, *40*(9-10), 2091–2121.

Wan, H., Rasch, P. J., Zhang, K., Qian, Y., Yan, H., & Zhao, C. (2014). Short ensembles: An efficient method for discerning climate-relevant sensitivities in atmospheric general circulation models. *Geoscientific Model Development Discussions*, *7*(5), 1961–1977.

Williams, K., Bodas-Salcedo, A., Déqué, M., Fermepin, S., Medeiros, B, Watanabe, M, et al. (2013). The Transpose-AMIP II experiment and its application to the understanding of Southern Ocean cloud biases in climate models. *Journal of Climate*, *26*(10), 3258–3274.

Winker, D., Pelon, J., Coakley Jr., J., Ackerman, S., Charlson, R., Colarco, P., et al. (2010). The CALIPSO mission: A global 3D view of aerosols and clouds. *Bulletin of the American Meteorological Society*, *91*(9), 1211–1229.

Wood, R. (2012). Stratocumulus clouds. *Monthly Weather Review*, *140*(8), 2373–2423.

Wood, R., & Bretherton, C. S. (2006). On the relationship between stratiform low cloud cover and lower-tropospheric stability. *Journal of Climate*, *19*, 6425–6432.

Wood, R., & Field, P. R. (2000). Relationships between total water, condensed water, and cloud fraction in stratiform clouds examined using aircraft data. *Journal of the Atmospheric Sciences*, *57*(12), 1888–1905.

Wood, R., Field, P., & Cotton, W. (2002). Autoconversion rate bias in stratiform boundary layer cloud parameterizations. *Atmospheric Research*, *65*(1-2), 109–128.

Zheng, X., Klein, S., Ma, H-Y, Bogenschutz, P, Gettelman, A, & Larson, V. (2016). Assessment of marine boundary layer cloud simulations in the CAM with CLUBB and updated microphysics scheme based on ARM observations from the Azores. *Journal of Geophysical Research: Atmospheres*, *121*, 8472–8492. https://doi.org/10.1002/2016JD025274

Zheng, X., Klein, S., Ma, H.-Y., Caldwell, P, Larson, V., Gettelman, A., & Bogenschutz, P. (2017). A cloudy planetary boundary layer oscillation arising from the coupling of turbulence with precipitation in climate simulations. *Journal of Advances in Modeling Earth Systems*, *9*, 1973–1993. https://doi.org/10.1002/2017MS000993